Heterogeneous damage in Li-ion batteries: Experimental analysis and theoretical modeling

Rong Xu[a], Yang Yang[b], Fei Yin[c], Pengfei Liu[a], Peter Cloetens[b], Yijin Liu[d], Feng Lin[e], Kejie Zhao[a],*

[a] School of Mechanical Engineering, Purdue University, West Lafayette, IN 47907, USA
[b] European Synchrotron Radiation Facility, Grenoble 38000, France
[c] School of Engineering Technology, Purdue University, West Lafayette, IN 47907, USA
[d] Stanford Synchrotron Radiation Lightsource, SLAC National Accelerator Laboratory, Menlo Park, CA 94025, USA
[e] Department of Chemistry, Virginia Tech, Blacksburg, VA 24061, USA

ARTICLE INFO

ABSTRACT

We assess the heterogeneous electrochemistry and mechanics in a composite electrode of commercial batteries using synchrotron X-ray tomography analysis and microstructure-resolved computational modeling. We visualize the morphological defects at multi-scales ranging from the macroscopic composite, particle ensembles, to individual single particles. Particle fracture and interfacial debonding are identified in a large set of tomographic data of active particles. Mechanical failure in the regime near the separator is more severe than toward the current collector. The active particles close to the separator experience deeper charge and discharge over cycles and thus are more mechanically loaded. The difference in the Li activity originates from the polarization of the electrolyte potential and the non-uniform distribution of the activation energy for the charge transfer reaction. We model the kinetics of intergranular fracture and interfacial degradation to confirm that the various Li activities are the major cause of the heterogeneous damage. The interfacial failure may reconstruct the conductive network and redistribute the electrochemical activities that render a dynamic nature of electrochemistry and mechanics evolving over time in the composite electrode. We further quantify the influence of the mechanical damage on the metrics of battery performance. We simulate the electrochemical impedance profile to build a relationship between the interfacial debonding and the impedance of electron transport and surface charge transfer. The mechanical failure disrupts the conduction path of electrons and results in significant polarization and capacity loss in batteries.

Published by Elsevier Ltd.

1. Introduction

Batteries occupy a privileged position in energy storage and emerge as a versatile and efficient option for the electrification of automotive transportation and integration of renewable energies. The global market by 2020 will be over $30 billion for Li-ion technology alone (Palacin and de Guibert, 2016). Reliability of Li-ion batteries is crucial *per se* in such large-scale applications and has a direct impact on the societal economics (Armand and Tarascon, 2008; Whittingham, 2008;

---

* Corresponding author.
  E-mail address: kjzhao@purdue.edu (K. Zhao).

Nomenclature

$\mathbf{i}_c$	Electric current density in carbon-binder matrix
K_c	Electric conductivity of carbon-binder matrix
ϕ_c	Electric potential in carbon-binder matrix
$\mathbf{i}_l$	Electric current density in electrolyte
K_l	Electric conductivity of electrolyte
ϕ_l	Electric potential in electrolyte
R	Gas constant
T	Temperature
F	Faraday's constant
f	molar activity coefficient of electrolyte
t_+	Transference number of cations
C_l	Li ion concentration in electrolyte
η	Activation overpotential
E_{eq}	Equilibrium potential for Li reaction
i_{BV}	Local charge transfer current density
i_0	Exchange current density
α_a	Anodic transfer coefficient
α_c	Cathodic transfer coefficient
k_a	Rate constant for anodic reaction
k_c	Rate constant for cathodic reaction
C_s	Li concentration in active materials
C_{s_max}	Max. Li concentration in active materials
C_{l_ref}	Reference Li ion concentration in electrolyte
i_{app}	Applied current density
$\mathbf{J}_l$	Li ion flux in electrolyte
$\mathbf{J}_s$	Li flux in active materials
D_l	Li ion diffusivity in electrolyte
D_s	Li diffusivity in active materials
C_{l_ini}	Initial Li ion concentration in electrolyte
C_{s_ini}	Initial Li concentration in active materials
L	Thickness of NMC electrode
L_s	Thickness of separator
W	Width of NMC electrode
$\boldsymbol{\sigma}$	Cauchy stress tensor
$\mathbf{C}$	Stiffness tensor
$\boldsymbol{\varepsilon}_{el}$	Elastic strain tensor
$\boldsymbol{\varepsilon}_{Li}$	Lithiation-induced strain tensor
$\mathbf{u}$	Displacement vector
Ω	Partial molar volume of Li atom
σ_h	Hydrostatic stress
σ_{eq}	Equivalent stress
ϵ_l	Matrix porosity
K_{c_eff}	Effective conductivity of carbon-binder matrix
K_{l_eff}	Effective conductivity of electrolyte
D_{l_eff}	Effective Li ion diffusivity in electrolyte
ξ	Frequency of perturbation
Z	Electrochemical impedance
ϕ_{app}	Applied potential
$\mathbf{i}_{out}$	Output current density
C_{dl}	Electric double layer capacitance
R_{int}	Debonding-induced interface resistance
σ_{c_i}	Cohesive strength between primary particles
G_{c_i}	Fracture toughness between primary particles
K_{int}	Interfacial stiffness
λ	Interfacial gap
λ_{ref}	Reference gap

$R_{\text{int\_ref}}$	Reference interface resistance
R_Ω	Ohmic resistance
R_{ct}	Charge transfer resistance
Z_w	Warburg impedance

Liu et al., 2018). It has become increasingly evident that the next-generation high-energy-density batteries will not be realized without understanding the degradation mechanism from the mechanics perspective (Zhao and Cui, 2016; Zhang et al., 2017). On one side, the repetitive volumetric strain in electrodes, ranging from a few percentages (graphite, layered/spinel/olivine oxides) to a few hundred percentages for the materials of ever-increasing energy density, disrupts the structural stability in batteries and deteriorates the capacity retention over cycles (Christensen and Newman, 2006; Shi et al., 2016; Xu et al., 2016; Ryu et al., 2018). On the other side, the mechanical stress influences the kinetics of electrochemical processes, such as mass transport, charge transfer, interfacial reactions, and phase transitions, thereby impacting the potential, capacity, and efficiency of batteries (Bower et al., 2011; Natsiavas et al., 2016; Xu and Zhao, 2016a, b; Zhang, 2017; Zhao et al., 2019).

Particle fracture and interfacial debonding are two major mechanisms accounting for the mechanical degradation in batteries. It seems inevitable to incur particle fracture in the cyclic deformation of the conventional intercalation-type electrodes (graphite, LiCoO$_2$, and Li$_2$Mn$_2$O$_4$) or conversion- and insertion-type high-capacity materials (Si, S, oxides) (Wang et al., 1999; Liu et al., 2012; Hao et al., 2014). For the current choice of high-capacity cathodes LiNi$_x$Mn$_y$Co$_z$O$_2$ (NMC, $x + y + z = 1$) and LiNi$_x$Co$_y$Al$_z$O$_2$ (NCA) in commercial Li-ion batteries, as-synthesized active materials often have a hierarchical structure that small primary particles of submicron size aggregate to form secondary particles of tens of micron meters. The fragmentation of secondary particles, a form of intergranular crack and decohesion between primary particle, has been observed as the major aging mechanism in NMC and NCA (Watanabe et al., 2014; Xu et al., 2017b; Ryu et al., 2018). Compared to particle fracture, the mechanical failure at the interface is relatively less studied because it is not easy to resolve the interfacial details between the active materials and the conductive agents in experiments. Nevertheless, recent experiments have confirmed that the relentless deformation of active particles upon Li reactions can cause fracture of the conductive matrix, break the weak bonding between the active material and most of conductive agents, and dynamically reconstruct the conductive network (Besnard et al., 2017; Müller et al., 2018). For the emerging technology of solid-state batteries, the mechanical compatibility between the electrodes and the solid electrolyte is a more prominent issue. Both the particle fracture and interfacial degradation contribute to the loss of active materials to the electron conduction path, increasing the ohmic and thermal resistance of the cell and reducing the capacity retention and energy output (Koerver et al., 2017). Furthermore, the mechanical failure disrupts the stability of the solid electrolyte interface (SEI). One consequence is that the swelling of electrodes causes repetitive breaking and re-forming of the SEI, consuming the lean Li source (Laresgoiti et al., 2015; Wang et al., 2018). The other is that the fresh surface created by fracture increases the site of the irreversible side reactions which causes the steady fade of cyclic efficiency (Lin et al., 2014; Mao et al., 2019).

There have been tremendous efforts in the past few years to understand the mechanical degradation of batteries where the intersection between mechanics and electrochemistry is of importance. Several recent papers summarized the state-of-the-art of the field (McDowell et al., 2016; Xu and Zhao, 2016a; Zhao and Cui, 2016; Zhang, 2017; Zhang et al., 2017; Wang et al., 2018; Zhao et al., 2019). On the experimental side, for example, the strain in the electrodes can be monitored by the optical microscope, transmission electron microscopy (TEM), and X-ray spectroscopy (Liu et al., 2011; Ebner et al., 2013a; Kondrakov et al., 2017), while the stress generation in a thin film of a single-phase or composite electrode can be accurately measured by the wafer curvature method (Sethuraman et al., 2010). Fracture of electrodes has been extensively observed by scanning electron microscopes (SEM), TEM, and X-ray micro- and nano-tomography (Wang et al., 1999; Liu et al., 2012; Hao et al., 2014). The precursor defect inception, accumulation, growth, and the resulting disorder of local chemical states are examined by the synchrotron X-ray analytical diagnosis and transmission techniques (Wei et al., 2018; Xia et al., 2018; Mao et al., 2019). Experimental characterizations on the interfacial debonding between the active phase and the inactive agents have attracted much recent interest in the context of solid-state batteries (Koerver et al., 2017). Among the experimental efforts, the development of in-situ techniques upon Li reactions, including scattering, spectroscopy, and microscopy, are particularly applauded (McDowell et al., 2012; Dolotko et al., 2014; Ma et al., 2016; Vasconcelos et al., 2017; Bak et al., 2018; Wu and Liu, 2018). A critical challenge in the mechanistic understanding of battery degradation is due to the intrinsic structural and compositional heterogeneity. Many of prior experiments have focused only on an idealized structure such as thin films and single particles, or on a local regime in the electrode of a limited size, which may lose the statistical representation of the overall chemomechanical behavior of electrodes at a large composite scale. To overcome this limitation, several groups recently develop a series of synchrotron-based analytical and tomography techniques to quantify the local chemical states of matters and map the mechanical failure of over thousands of particles upon cell cycles (Ebner et al., 2013b; Lin et al., 2017; Li et al., 2018; Yang et al., 2019). Results have shown that a major characteristic of both electrochemistry and mechanics in a commercial electrode is the heterogeneity – significant spatial and temporal variations in Li concentration, stress, and damage, exist at the local positions in a composite (Müller et al., 2018; Yang et al., 2019). The study on the heterogeneous chemomechanics and damage in batteries is at the early stage. Many

basic questions, such as, what are the origins of the spatial and temporal heterogeneity, how does the heterogeneity incur the damage in batteries, how to identify the statistically representative events in the particle ensemble, how to detect the minority phases in a large set of database for numerous particles, and how does the heterogeneous behavior of electrodes influence the overall capacity and cyclic performance of batteries, are largely unclear. The same challenge remains for the theoretical development and computational modeling. A basic idea in mechanics is to treat the Li reaction induced strain as an eigenstrain, and to calculate the diffusion-induced stress using the same theory of thermal stresses (Prussin, 1961; Huggins and Nix, 2000; Christensen and Newman, 2006; Ryu et al., 2011). The electric field in batteries evolves by the constitutive equations of electron transport, mass diffusion, charge transfer kinetics, and redox reactions in electrodes (Doyle et al., 1993; Bower et al., 2011; Newman and Thomas-Alyea, 2012). The fields of mechanics and electrochemistry are coupled by considering the stress-regulated Li diffusion and surface charge transfer (Stein et al., 2016; Lu et al., 2018; Wu and Lu, 2019). Further extended theories include the stress-regulated interfacial reactions, coupled plasticity and chemical reactions (termed as reactive flow), and the coupling between Li transport and fracture (termed as corrosive fracture) in electrodes (Zhao et al., 2012a, 2012b; Brassart and Suo, 2013; Xu and Zhao, 2018). A common approach to apply the theories in numerical modeling is to use a simplified 1D model or a homogenized pseudo-2D (P2D) model. The simplified 1D models often use single freestanding particles or thin films (Christensen and Newman, 2006; Anand, 2012; Klinsmann et al., 2016). Homogenized P2D models refer to the models separating two length scales: The electron and Li transports are assumed to occur in 1D in the thickness direction of the electrode, while the active material to accommodate Li insertion is simplified as a spherical particle (Doyle et al., 1993; Fuller et al., 1994). In commercial batteries, both the cathode and anode are composites of high heterogeneity at the nano- to microscale, consisting of active particles of different sizes and irregular shapes, a matrix composed of polymer binders and additives, and pores filled with the electrolyte. The simplified models are useful to capture the first-order effect of the stress and electrochemistry in batteries, but, the predictions on Li concentrations, the stress field, and mechanical failure from the idealized models can be substantially different from that of the real composite configurations. For instance, recent studies (Chung et al., 2011; Hun et al., 2011; Lim et al., 2012; Roberts et al., 2014; Mendoza et al., 2016; Mai et al., 2019) have suggested: (i) The stress field and Li distribution are strongly affected by the local details of the microstructure and the mechanical interactions of the different components in the electrodes, (ii) The percolated bicontinuous network of reconstructed particles shows significantly higher stresses than that in single isolated particle, (iii) The mechanical properties of binders, particularly the yield stress and elastic modulus, play an important role in determining the average stresses developed in the electrode, and (iv)The state of charge in the active particles is highly inhomogeneous depending on the size, shape, and distribution of the particles. The effective capacity of electrodes is not linearly scaled with the mass of the active materials, but is limited by the inhomogeneous storage of Li.

It is a grand challenge to model the fully coupled mechanics and electrochemistry in a real and complex geometry of composite electrodes. Nevertheless, the recent development of 3D tomography reconstruction techniques, such as X-ray nano-tomography, transmission microscopy, and focused ion beam/scanning electron microscope (FIB/SEM), makes it possible to reconstruct the microstructure of commercial electrodes with sufficient nanoscale details (Song et al., 2015; Lin et al., 2017; Yang et al., 2019). The microstructure-resolved models can be imported into computational programs to mimic the electrode behavior under the battery operation condition. In this work, we combine the merits of the advanced 3D tomographic visualization and the microstructure-resolved modeling to examine the heterogeneous electrochemistry, stress, fracture, and interfacial debonding in a commercial electrode. We focus on the spatial and temporal variations from the macroscopic level of composites down to single particles. We must clarify that significant details of the experiments on the synchrotron X-ray analysis are reported in a separate work (Yang et al., 2019). Rather than repeating the experimental details, the key focus of this paper is on the theoretical modeling and understanding of the heterogeneous damage in batteries from the mechanics perspective. Since the experiments and modeling are closely related, we will start with the experimental observations which serve as a motivation of the study and later will be quantitatively compared with the numerical modeling. The experimental results in this paper were not included in our previous work (Yang et al., 2019). In Section 2, we introduce the setup of experiments using the X-ray phase contrast tomography to probe a large set of active particles throughout a cycled NMC cathode. Fracture of NMC particles is categorized by the degree of damage in individual particles using the machine learning algorithm. We manage to resolve the different phases in the conductive matrix which is an unprecedented capability in the tomographic analysis. Interfacial debonding between NMC particles and carbon blacks is clearly visualized and spatially quantified. In Section 3, we use computational modeling to gain in-depth understanding of the mechanism responsible for the heterogeneous damage. We develop a finite element program based on a fully coupled electro-chemo-mechanics theory which accounts for the stress effect in surface charge transfer and diffusion kinetics. We apply the theory to a 3D reconstructed model to simulate the full fields of electrochemistry and mechanics in the NMC cathode. The model features the strong effect of mechanical stresses on the capacity, voltage, and cyclic efficiency of batteries at the fast charging condition. We show the significant heterogeneity in Li distributions, stresses, NMC particle fracture, and interfacial debonding upon Li reactions. Furthermore, we target to draw a quantitative relationship between the mechanical degradation and the metrics of battery performance such as electrochemical impedance, voltage response, and deliverable capacity. Such a quantitative correlation is missing information in the field of studies and will be important for the design of electrodes of optimum mechanical stability and electrochemical performance. The numerical results agree very well with our experimental observations.

2. Experiments on heterogeneous damage in NMC cathode

2.1. Experimental methods

2.1.1. Sample preparation

NMC ($LiNi_{0.6}Mn_{0.2}Co_{0.2}O_2$) particles were synthesized through a co-precipitation method described in the previous work (Wei et al., 2018). NMC composite cathodes were prepared via a slurry-based casting method. NMC active particles (90 wt.%), acetylene carbon (5 wt.%), and polyvinylidene difluoride (5 wt.%, dissolved in N-Methyl-2-pyrrolidone) were mixed and then casted on a carbon-coated aluminum foil with a mass loading of 7.7 mg/cm^2. The as-coated electrodes were dried in a vacuum oven overnight at 120 °C and then stored in argon-filled glovebox (moisture and oxygen levels less than 1.0 ppm) for several days before use. Next, electrodes were assembled into coin cells in glovebox for electrochemical testing. The NMC electrode, Li foil, and Celgard2500 membrane were used as the cathode, anode, and separator, respectively, in the CR-2032 type coin cells. The electrolyte was composed of 1 M LiPF$_6$ salt dissolved in ethylene carbonate/ethyl methyl carbonate of 1:2 volume ratio (EC/EMC, 1:2). All assembled cells were placed to rest overnight to ensure complete wetting before the electrochemical test. All coin cells were cycled for 10 times at a rate of 5C at 23 °C. The coin cells were then disassembled at the charged state of 4.3 V in the glovebox and the NMC electrodes were collected for characterizations.

2.1.2. X-ray phase contrast tomography

We used a synchrotron hard X-ray contrast tomography with high spatial resolution to track the morphological evolution of the microstructure of NMC electrodes. Morphological mapping of the NMC electrodes was conducted using an ID16A-NI nano-imaging beamline in the European Synchrotron Radiation Facility (ESRF) in Grenoble, France (Cesar da Silva et al., 2017). This beamline offers a unique combination of nanofocus ($\sim$20 nm) and a high photon flux (up to 1012 photons/s at $\Delta E/E \sim 1\%$), which enables nano-tomography detection with a high energy of 17 keV as well as a large field of view (FOV) with 100 nm and 70 nm voxel size. The free space propagation of the X-ray beam indicates that the contrast of images, i.e. the phase contrast of the complex refractive index, is determined by the material electron density. Therefore, by measuring the Fresnel diffraction patterns at different effective propagation distances, the phase maps of the sample can be retrieved via holographic reconstruction, so-called phase retrieval procedure implemented in the GNU Octave software (Cloetens et al., 1999). In the experiments, the NMC sample electrode was placed downstream of the Kirkpatrick-Baez (KB) focus and the magnified radiographs were recorded by an X-ray detector using a FReLoN charged-coupled device (CCD) with a 2048 $\times$ 2048 binned pixels array. 1500 projections were acquired within one tomography scan with 0.2 s exposure time at 70 nm pixel size. A series of tomography scans at different focus distances were acquired to construct one holotomography scan. The 2D phase mapping retrieved from the angular projections was then used as input for a tomographic reconstruction via the filtered back projection (FBP) algorithm method (Mirone et al., 2014).

2.1.3. X-ray spectro-tomography

We conducted X-ray spectro-tomography scan on the charged NMC particles using the transmission X-ray microscopy (TXM) at beamline 6-2C at Stanford Synchrotron Radiation Lightsource of the SLAC National Accelerator Laboratory. NMC particles were loaded in a helium-filled quartz capillary (100 μm in diameter and 10 μm in wall thickness) for imaging. The typical exposure time for single images is 0.5 s and the nominal spatial nano-resolution is about 30 nm. More details of the synchrotron beamline configuration and the concept of the X-ray spectro-tomography can be found in the literature (Meirer et al., 2011). In the 3D spectro-tomography scan, the energy of the incident X-rays was scanned from 8200 eV to 8630 eV to cover the absorption K-edges of Ni. The tomography was performed at 68 different energy points. In the near edge region (8330 eV to 8355 eV), we chose the energy step at 1 eV to ensure sufficient energy resolution. The pre-edge and post-edge regions were scanned with larger energy steps of 10 eV to cover a relatively wide energy window for normalization of the spectra. The TXM data processing was performed using an in-house developed software package TXM-Wizard (Rueden et al., 2017). The segmentation and visualization of the 3D data were carried out using a commercial software package Avizo.

2.1.4. Scanning electron microscopy

The microstructure of NMC electrode was imaged using SEM (QUANTA 3D FEG Dual Beam, FEI) at 5 kV. The cross-section of the pristine and cycled NMC electrodes were imaged after the focus ion beam (FIB) milling. An accelerating voltage of 30 kV and a beam current of 20 nA were used for the FIB milling.

2.2. Results and discussion

We detect the morphology and defects in the NMC electrode using multi-scale imaging and diagnosis techniques as demonstrated in Fig. 1. Fig. 1(a) illustrates the rendering of 3D tomographic data, from the particle ensemble down to single particles, in an NMC electrode cycled after 10 times at a charging rate of 5C. The panel shows an overview of our multi-scale approach, which includes the phase contrast micro-tomography data of the composite (450 nm pixel size), a magnified region of interest (phase contrast nano-tomography data, 70 nm pixel size), and a single particle (transmission X-ray microscopic data, 30 nm pixel size). The microstructural details of the single particle can be further resolved through
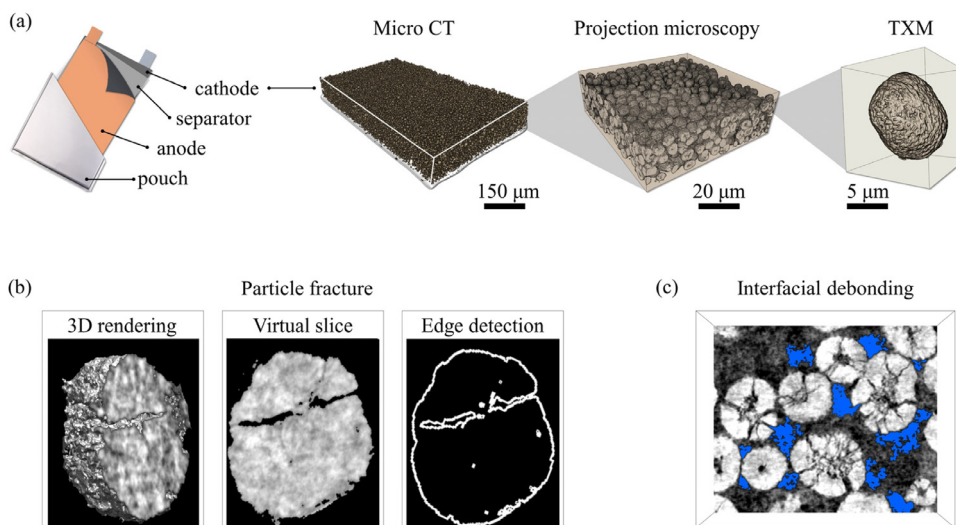
Fig. 1. Multi-scale imaging and diagnosis on the morphological defects in an NMC cathode of Li-ion batteries. Panel (a) illustrates the tomographic data from the composite film down to a single active particle. Panel (b) shows the 3D rendering, the central virtual slice, and the edge detection of an arbitrarily selected NMC secondary particle. The edge detection identifies and segments voxels over the particle surface where the cracks are outlined. (c) Visualization of the interfacial debonding and the resulted detachment of the active particles from the conductive network. The blue color highlights the void regions based on the image contrast in the slice of the cycled NMC cathode. (For interpretation of the references to color in this figure legend, the reader is referred to the web version of this article.)

a 3D cross-sectional rendering, as illustrated by the first panel of Fig. 1(b), from which we can see a major crack induced by the Li cycles. To quantify the particle fracture more precisely, we develop an advanced approach for crack detection. We first apply a mild median filtering (2 pixel) to the 3D tomogram to improve the signal-to-noise ratio. The projected cross-section of the single particle after mild median filtering is illustrated in the second panel of Fig. 1(b). Although the filtering slightly sacrifices the spatial resolution, the high contrast in the particle edge and fracture profile is not significantly influenced. After filtering, the particle edge and crack profile can be automatically detected by a Canny edge detection algorithm integrated in the software ImageJ (Canny, 1987; Rueden et al., 2017), as shown in the third panel of Fig. 1(b). Last, we use the detected particle edge to automatically isolate individual particles from the whole electrode, and then rely on the detected crack profile to quantify the degree of particle damage. Interfacial debonding between the NMC particles and the conductive matrix can be also visualized via the phase contrast methodology, which offers excellent sensitivity to the local electron density and distinguishes the three different phases in the composite electrode (active NMC, inactive carbon/binder, and void/pores). Fig. 1(c) demonstrates the interfacial debonding and the resulted detachment of the active particles from the conductive network in a slice of the cycled NMC cathode. The blue color highlights the void regions based on the phase contrast. The nanoscale feature of the separation of the active particles from the conductive network and the pore regimes are clearly detected in our data.

Another significant feature of the X-ray phase contrast nano-tomography is that this technique can collect morphological details for over a thousand active particles with spatial resolution of ∼70 nm within one scan. Such a large database offers very rich particle informatics. It allows us to examine in detail the mechanical degradation of commercial batteries not only at single particles level with sufficient details but also at the large composite level with more meaningful statistical analysis. We determine the spatial distribution of particle fracture in the cycled NMC sample. Fig. 2(a) illustrates the 3D profile of particle fracture in a selected regime of $150\,\mu m$ (length) $\times$ $150\,\mu m$ (width) $\times$ $40\,\mu m$ (thickness). NMC particles are color-coded according to the degree of damage – red represents the severely fractured particles and blue represents the least damaged particles. The degree of particle damage was estimated using the smallest eigenvalue based on the structure tensor analysis. We applied a moving 3D window (with the size similar to individual particles) to extract the local structure tensor, which indicates the local orientation anisotropy. While the largest eigenvalues represent the dominant orientation, which are the particle circular edges; the smallest eigenvalues detect the features that are orthogonal to the largest eigenvalues, i.e. the fractures. These smallest eigenvalues were averaged within the moving 3D window to calculate the degree of local fractures for every single particle throughout the entire volume (Rao and Schunck, 1991; Weickert, 1999; Meijering, 2019). It is evident that the electrochemical cycle induces a depth-dependent pattern of particle fracture. The NMC particles near the separator experience more severe damage than those near the current collector at the bottom of the cell. To make a quantitative comparison, we show the projected lateral slices at the two locations in the right panel of Fig. 2(a). The statistics is following: ∼7.1% of particles are least damaged and ∼58.6% of particles are severely damaged for the layer near the separator, while ∼49.2% of particles are least damaged and ∼13.8% of particles are severely damaged for the layer near the current collector. We use a similar strategy to evaluate the spatial distribution of interfacial debonding incurred in the electrode. We select the same two lateral slices in the electrode of different depth in the thickness direction, one near
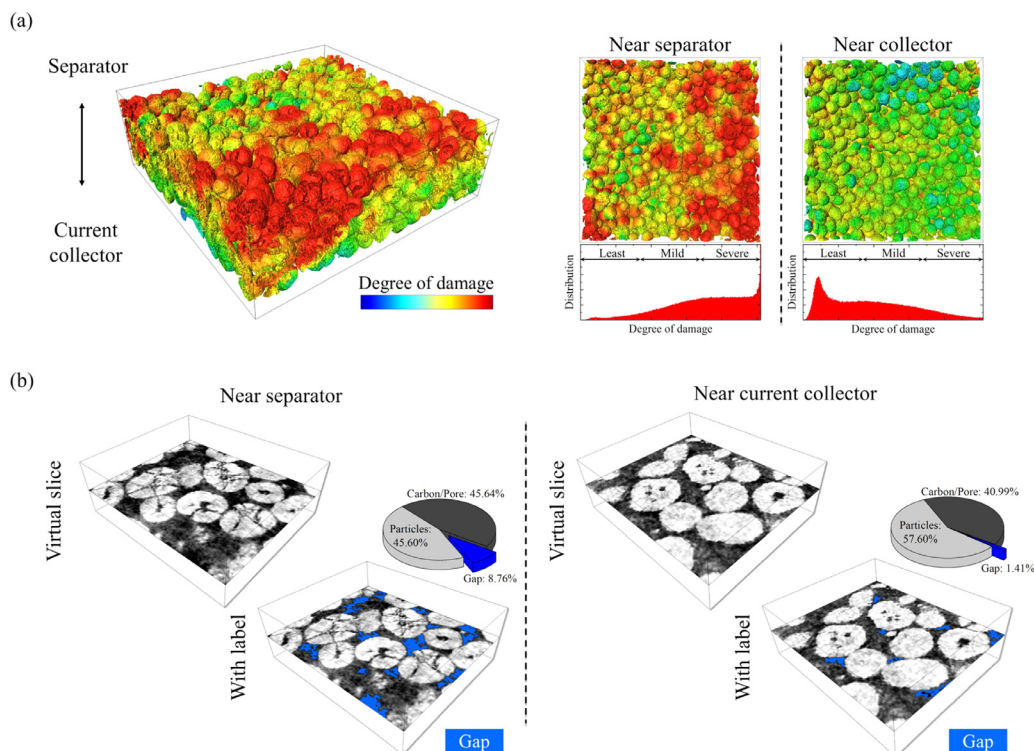
Fig. 2. Spatially heterogeneous damage, including particle fracture and interfacial debonding, in the NMC cathode after 10 cycles with the cyclic rate of 5C. (a) The 3D profile of particle fracture in a selected regime of $150 \times 150 \times 40 \, \mu m$. NMC particles are color-coded according to the degree of damage – red represents the severely fractured particles and blue represents the least damaged particles. Right panel shows the lateral slices near the separator versus near the current collector of the electrode. (b) The depth-dependent interfacial debonding between the NMC particles and the conductive matrix. The two panels show the comparison in the particle morphology as well as the color-coded gaps in the virtual slices near the separator versus near the current collector. (For interpretation of the references to color in this figure legend, the reader is referred to the web version of this article.)

the separator and the other near the current collector. The morphological features of these two slices are presented in the upper panels of Fig. 2(b). The blue color-coded gaps represent the interfacial debonding between the NMC particles and the conductive matrix as shown in the lower panels of Fig. 2(b). The statistics of the areal fraction of interfacial debonding in the slices is calculated as follows: ∼8.8% of the imaged area is debonded for the layer near the separator, while ∼1.4% is degraded near the current collector. It is clear that the interfacial failure is of significant spatial heterogeneity and the pattern coincides with the particle fracture. The particles near the separator with a high degree of fracture tend to lose contact with the conductive network. Such heterogeneous damages, including both the particle fracture and loss of interfacial contact, are due to the difference in the state of charge in NMC particles which results in different Li activities across the depth of the electrode in the same charging/discharging process. The mechanistic understanding of the heterogeneous damage remains answered. Meanwhile, the dynamic evolution of the heterogeneous damage, their interference with the electron/ion conduction, and therefore the influence on the material states in later cycles are questions to be systematically studied. The intertwined electrochemical processes and mechanical degradation enrich the forefront the electro-chemo-mechanics and are of significance for the optimum design of battery reliability.

3. Theoretical modeling on the heterogeneous electrochemistry and mechanics

3.1. Theoretical framework

In a commercial Li-ion battery, three different components coexist in the composite electrode, as shown in Fig. 3(a) and (b). Active particles are embedded in the porous matrix of carbon additives and polymeric binders. Liquid electrolyte is soaked in the porous matrix to provide an interconnected diffusion channel for Li ions. The porous carbon matrix is used to form the electric conductivity network of the electrode, and at the same time, to physically hold the active particles. The working principle of a Li-ion battery using an NMC cathode paired with a Li metal anode is sketched in Fig. 3(c). During charging, Li extracts from NMC and splits into Li ions and electrons on the particle surface. Electrons flow through the conductive carbon-binder network to the cathode current collector, and transport through the external circuit to the anode side. To maintain electroneutrality, Li ions diffuse through the electrolyte in the pore space of electrodes and separator, and reach the anode side to neutralize the electrons. The above processes are reversed if the battery is under discharging. The
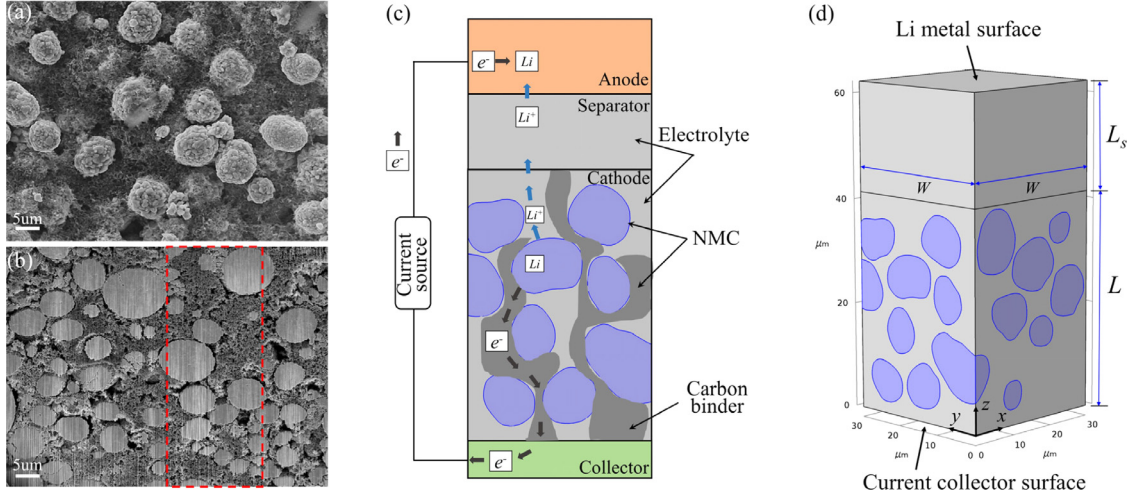
Fig. 3. Microstructural features of a commercial NMC cathode and the model we construct for finite element modeling. (a) and (b) show the top and cross-section views of the composite NMC, respectively. (c) Sketch of the working principle of a half-cell composed of an NMC cathode and a Li metal anode. (d) A half-cell configuration used to model the electro-chemo-mechanical behavior of the NMC cathode. The model includes a current collector, a porous cathode, an electrolyte, and a Li metal anode. The thicknesses of the cathode current collector and Li metal anode are set as zero in the model.

electrochemical processes in batteries are well described by the theory developed by Newman et al. (Doyle et al., 1993; Newman and Thomas-Alyea, 2012). Mechanics takes place when Li ions are inserted into or extracted from the active materials. The volumetric deformation generates a field of stress and subsequent mechanical degradation in the electrode. In this work, we use a fully coupled electro-chemo-mechanics theory which includes the kinetics of electron and ion transports in different components of the electrode, the deformation kinematics and stresses of the composite, and the stress effect on Li diffusion and charge transfer reactions. The theory forms a foundation of the computational modeling.

3.1.1. Electric potential

In the conductive matrix, the electric current density $\mathbf{i}_c$ at a given location is defined by the Ohm's law,

$$\mathbf{i}_c = -K_c \nabla \phi_c, \tag{1}$$

where K_c and ϕ_c denote the electric conductivity and potential in the carbon-binder matrix, respectively. Due to the charge conservation, the electric current density field follows

$$\nabla \cdot \mathbf{i}_c = 0. \tag{2}$$

In the pore space filled with liquid electrolyte, the electric current density is governed by the migration and diffusion of the charged species. Assuming that the electrolyte solvent remains static and Li ion is the only moving species, Newman et al. (Doyle et al., 1993; Newman and Thomas-Alyea, 2012) derived the electric current density as

$$\mathbf{i}_l = (-K_l \nabla \phi_l) + \frac{2K_l RT}{F}\left(1 + \frac{\partial \ln f}{\partial \ln C_l}\right)(1 - t_+)\nabla \ln C_l, \tag{3}$$

where K_l is the electrolyte conductivity, ϕ_l the electric potential in the electrolyte, and C_l the Li concentration in the electrolyte. R is the gas constant, T the temperature, F the Faraday's constant, t_+ the transference number of the cation, and f the mean molar activity coefficient of the electrolyte. Charge conservation in the electrolyte requires the electric current density field to be free of divergence,

$$\nabla \cdot \mathbf{i}_l = 0 . \tag{4}$$

At the interface between the electrolyte and the active material, the electrochemical charge transfer severs as a boundary source or sink of the electric current. The charge transfer rate is related with the overpotential η, which is defined as,

$$\eta = \phi_c - \phi_l - E_{eq} - \frac{\Omega \sigma_h}{F}, \tag{5}$$

where E_{eq} is the equilibrium potential for Li reaction in the active material, Ω the partial molar volume of Li atom in the active material, and σ_h is the hydrostatic stress, expressed as $(\sigma_{11} + \sigma_{22} + \sigma_{33})/3$. It is noted that the E_{eq} and σ_h in Eq. (5) are both calculated at the surface of the active materials. The last term in Eq. (5) includes the stress effect on the charge transfer reaction which accounts for the shift of the equilibrium potential by stresses. Butler-Volmer equation is typically used to describe the relationship between the charge transfer rate and the overpotential (Newman and Thomas-Alyea, 2012),

$$i_{BV} = i_0\left(\exp\left(\frac{\alpha_a F\eta}{RT}\right) - \exp\left(-\frac{\alpha_c F\eta}{RT}\right)\right), \tag{6}$$

where i_{BV} is the local charge transfer current density at the interface between the electrolyte and the active material, α_a the anodic transfer coefficient, α_c the cathodic transfer coefficient, and i_0 the exchange current density, defined as,

$$i_0 = F(k_c)^{\alpha_a}(k_a)^{\alpha_c}(C_{s\_max} - C_s)^{\alpha_a}(C_s)^{\alpha_c}\left(\frac{C_l}{C_{l\_ref}}\right)^{\alpha_a}, \tag{7}$$

where k_c and k_a are the rate constants for the cathodic and anodic reactions, respective. C_s denotes the bulk Li concentration in the active material. C_{s_max} and C_{l_ref} represent the maximum Li concentration in the active material and a reference Li concentration in the electrolyte, respectively.

Due to the electroneutrality, the number of Li ions diffusing through the electrolyte during charging must be equal to the number of electrons carried by the conductive agents. Therefore, the boundary conditions at the interfaces between the electrolyte and the active material, and between the conductive matrix and the active material, can be written as,

$$\begin{aligned}\mathbf{i}_l \cdot \mathbf{n}_l &= -i_{BV}, \\ \mathbf{i}_c \cdot \mathbf{n}_c &= i_{BV},\end{aligned} \tag{8}$$

where $\mathbf{n}_l$ is the unit normal vector pointing from the electrolyte to the active material and $\mathbf{n}_c$ is the unit normal vector pointing from conductive matrix to the active material. Other boundary conditions for the electric field we use in the half-cell model in Fig. 3(c) are set as follows,

$$\begin{aligned}\mathbf{i}_l \cdot \mathbf{n}_{side} &= 0 \text{ at } x = 0, \quad x = W, \ y = 0, \text{ and } y = W; \\ \mathbf{i}_c \cdot \mathbf{n}_{side} &= 0 \text{ at } x = 0, \quad x = W, \ y = 0, \text{ and } y = W; \\ \mathbf{i}_l \cdot \mathbf{n}_{cc} &= 0 \text{ at } z = 0; \\ \mathbf{i}_c \cdot \mathbf{n}_{cc} &= -i_{app} \text{ at } z = 0; \\ \mathbf{i}_l \cdot \mathbf{n}_{Li} &= i_{app} \text{ at } z = L + L_s; \\ \mathbf{i}_c \cdot \mathbf{n}_{cs} &= 0 \text{ at } z = L; \\ \phi_c &= 0 \text{ at } z = L + L_s,\end{aligned} \tag{9}$$

where $\mathbf{n}_{side}$ is the unit normal vector pointing outside from the model, $\mathbf{n}_{cc}$ is the unit normal vector pointing from the cathode to the current collector, $\mathbf{n}_{Li}$ from the separator to the Li metal anode, and $\mathbf{n}_{cs}$ from the cathode to the separator. i_{app} is the applied current density at the current collector.

3.1.2. Li concentration

Li transport in both the electrolyte and the active material is solved using diffusion kinetics. Li transport follows,

$$\begin{aligned}\frac{\partial C_l}{\partial t} + \nabla \cdot \mathbf{J}_l &= 0, \\ \frac{\partial C_s}{\partial t} + \nabla \cdot \mathbf{J}_s &= 0.\end{aligned} \tag{10}$$

For Li ions in the electrolyte, Li flux is denoted as $\mathbf{J}_l$. In addition to the diffusion process, Li migration in the electrolyte must be accounted into the flux,

$$\mathbf{J}_l = -D_l \nabla C_l + \frac{\mathbf{i}_l t_+}{F}, \tag{11}$$

where D_l is the Li ion diffusivity in the electrolyte. For Li transport in the active material, Li flux is denoted as $\mathbf{J}_s$,

$$\mathbf{J}_s = -D_s\left(\nabla C_s - \frac{\Omega C_s}{RT}\nabla \sigma_h\right), \tag{12}$$

where D_s is the Li diffusivity in the active material. Eq. (12) includes the stress effect on the kinetics of Li transport, in which the driving force for Li diffusion is determined by the gradients of Li concentration and the hydrostatic stress.

According to the charge conservation, the boundary conditions at the interfaces between the electrolyte and the active material can be written as,

$$\begin{aligned}\mathbf{J}_l \cdot \mathbf{n}_l &= -\frac{i_{BV}}{F}, \\ \mathbf{J}_s \cdot \mathbf{n}_l &= -\frac{i_{BV}}{F},\end{aligned} \tag{13}$$

Other boundary conditions for Li transport in the half-cell model in Fig. 3(c) are summarized as follows,

$$\begin{aligned}\mathbf{J}_l \cdot \mathbf{n}_{side} &= 0 \text{ at } x = 0, \ x = W, \ y = 0, \text{ and } y = W; \\ \mathbf{J}_s \cdot \mathbf{n}_{side} &= 0 \text{ at } x = 0, \ x = W, \ y = 0, \text{ and } y = W; \\ \mathbf{J}_l \cdot \mathbf{n}_{cc} &= 0 \text{ at } z = 0; \\ \mathbf{J}_l \cdot \mathbf{n}_{Li} &= \frac{i_{app}}{F} \text{ at } z = L + L_s.\end{aligned} \tag{14}$$

Initial conditions of Li concentration in the electrolyte and active material are given by C_{l_ini} and C_{s_ini} at $t = 0$.

3.1.3. Mechanical deformation

The stress field in both the active material and the inactive matrix is governed by the equation of mechanical equilibrium,

$$\nabla \cdot \boldsymbol{\sigma} = 0, \tag{15}$$

The stress $\boldsymbol{\sigma}$ is calculated by the Hook's law, $\boldsymbol{\sigma} = \mathbf{C} : \boldsymbol{\varepsilon}_{\text{el}}$, where $\mathbf{C}$ is the stiffness matrix and ε_{el} the elastic strain. For a representative material element, the total strain ε, elastic strain ε_{el}, and lithiation (delithiation) induced strain ε_{Li} follow the kinematic relationship,

$$\boldsymbol{\varepsilon} = \boldsymbol{\varepsilon}_{\text{el}} + \boldsymbol{\varepsilon}_{\text{Li}} . \tag{16}$$

The total strain ε is correlated with the displacement field u as

$$\boldsymbol{\varepsilon} = \frac{1}{2}\left((\nabla \mathbf{u})^{\text{T}} + \nabla \mathbf{u}\right) . \tag{17}$$

Lithiation (delithiation) induced strain ε_{Li} is assumed to be proportional to the Li concentration in the active material C_s,

$$\boldsymbol{\varepsilon}_{\text{Li}} = \frac{1}{3}\Omega(C_s - C_{s\_\text{ini}})\mathbf{I}, \tag{18}$$

where C_{s_ini} is the initial Li concentration in the host material at the stress-free state. This equation assumes an isotropic expansion in each direction upon Li reactions. This assumption is not correct to treat the deformation in a single crystal of layered cathode. Nevertheless, the isotropic assumption is not unreasonable to calculate the strain in the granular NMC secondary particles which are composed of agglomerates of primary particles. We will use the isotropic deformation to calculate the deformation in NMC secondary particles for simplicity, and will use the rigorous anisotropic deformation in NMC primary particles to model the intergranular fracture incurred between the primary particles.

The boundary conditions for the mechanical deformation are prescribed as follows,

$$\begin{aligned} &\mathbf{u} \cdot \mathbf{n}_{\text{side}} = 0 \text{ at } x = 0, \ x = W, \ y = 0, \ \text{and} \ y = \ W; \\ &\mathbf{u} \cdot \mathbf{n}_{\text{cc}} = 0 \text{ at } z = 0. \end{aligned} \tag{19}$$

3.2. Numerical method

We implement the coupled electro-chemo-mechanics theory outlined in Section 3.1 into a finite element program in COMSOL Multiphysics (Version 5.3). The built-in time-dependent solver MUMPS (MUltifrontal Massively Parallel sparse direct Solver) is used to solve the weak forms of the kinematics of deformation as well as the kinetics of Li diffusion and electron transport. More details about the implementation of the theory in the computational program can be found in our previous work (Xu and Zhao, 2018).

We apply the finite element method on a 3D microstructure-resolved model to simulate the electrochemistry and mechanics in a commercial electrode. We reconstruct the 3D composite electrode based on the X-ray phase contrast tomography data, Fig. 4(a). An arbitrarily selected region ($180 \times 60 \times 40 \, \mu$m, 602 particles) in the electrode is selected as the region of interest (ROI), Fig. 4(b). To balance the computational cost and structural representativity, 1/12 of the ROI ($30 \times 30 \times 40 \, \mu$m, 48 particles) is selected as a representative volume element (RVE), Fig. 4(c). The software Avizo is used to convert the 3D tomography data into a Standard Tessellation Language (STL) data which can be imported into COMSOL. In the conversion, Laplacian smoothing filter in the open-source tool MeshLab is used to smooth the surface of NMC particles, since the default surface morphology from the tomography data is often far too fine for simulation. More details about the 3D reconstruction from the tomography data are described in our previous work (Xu et al., 2016).

We carefully compare the statistical features of the reconstructed RVE in Fig. 4(c) with the nano-tomography data of ROI in Fig. 4(b), to ensure that the RVE is truly representative to the microstructural details of the NMC electrode. The volume fractions of active particles in RVE and ROI are close, 40.0% and 40.1% in each. In addition, geometrical information, including the coordinate of the particle center and the equivalent particle diameter for all NMC particles, is extracted for a more detailed statistical analysis. Fig. 4(d)–(f) show the probability distribution functions of the particle volume, the effective particle diameter, and the nearest neighbor distance (surface to surface) in the RVE and ROI, respectively. The statistical comparison confirms that the selected RVE maintains the same microstructural features of the NMC composite and thus the output can reasonably represent the chemomechanical behavior of the electrode at the large scale.

We incorporate the reconstructed RVE model into a half-cell configuration (Fig. 3(d)) for modeling the electrochemistry and mechanics fields. Due to the high electric conductivity of Li metal, the thickness of Li metal anode has a negligible effect on the cell voltage and polarization, and thus is set as zero. To simulate the galvanostatic charging and discharging, a constant current is applied at the cathode current collector side and its magnitude is determined by the specific cyclic rate.

In the simulation, the empty space of the RVE is filled with a homogenized matrix which consists of the electrolyte and the carbon-binder matrix. Considering that the matrix is impermeable for Li ions and that the liquid electrolyte is insulating for electrons, only the electron transport is considered in the carbon-binder matrix and only the Li ion transport is allowed in the electrolyte. The electrolyte and the conductive matrix can be usually treated as a superimposed continuum. In this
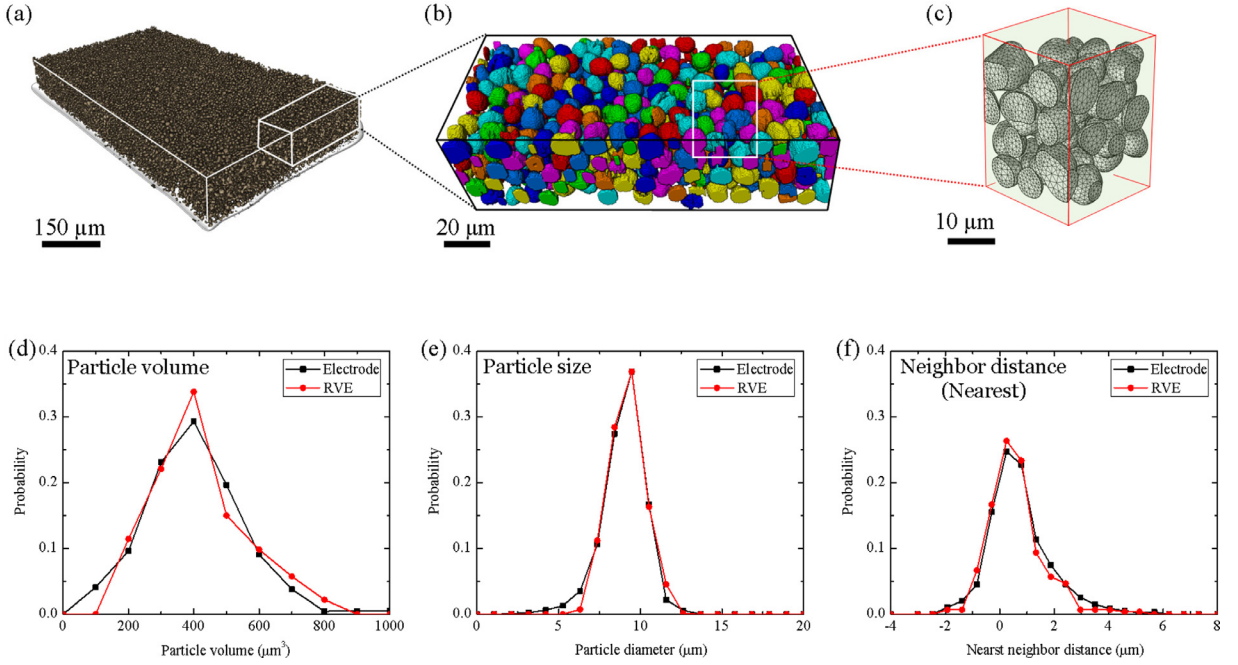
Fig. 4. Reconstruction of the 3D composite model and statistical features of the computational model. (a) The micro-tomography data of a commercial NMC electrode with the pixel size of $0.65\,\mu$m. (b) 3D rendering of the X-ray nano-tomography data (pixel size 75 nm) for an arbitrarily selected regime. (c) A representative volume element (RVE) extracted from the nano-tomography data in (b). The model size is $30 \times 30 \times 40\,\mu$m. (d–f) Statistical analysis of the RVE in comparison with the nano-tomography data in (b) in terms of the probability distribution functions of the particle volume, the effective particle diameter, and the nearest neighbor distance.

circumstance, the mass balance of Li ions in the electrolyte component of the homogenized matrix (first formula in Eq. (10)) should be modified as,

$$\epsilon_l \frac{\partial C_l}{\partial t} + \nabla \cdot \mathbf{J}_l = 0, \tag{20}$$

where ϵ_l is the volume fraction of electrolyte in the homogenized matrix (i.e. porosity of the matrix). In the commercial NMC electrode in Fig. 4(b) and the reconstructed RVE in Fig. 4(c), the volume fractions of active particles, the liquid electrolyte, and the carbon-binder matrix are about 40%, 30%, and 30%, respectively, resulting in the porosity of the homogenized matrix ϵ_l being 0.5. This relatively high porosity is because we do not calender the electrodes to avoid any prior mechanical damage in NMC particles caused by the calendering process. The variation of the matrix porosity induced by the small deformation of NMC particles has been ignored in the calculations. In addition to the mass balance equation, the pure phase transport properties including the matrix conductivity K_c in Eq. (1), the electrolyte conductivity K_l in Eq. (3), and the ionic diffusivity in the electrolyte D_l in Eq. (11) should be replaced by the effective transport properties in the homogenized matrix. The Bruggeman relationship (Tjaden et al., 2016) is employed to evaluate the effective transport properties,

$$
\begin{aligned}
K_{c\_\text{eff}} &= (1 - \epsilon_l)^{1.5} K_c, \\
K_{l\_\text{eff}} &= \epsilon_l^{1.5} K_l, \\
D_{l\_\text{eff}} &= \epsilon_l^{1.5} D_l,
\end{aligned}
\tag{21}
$$

3.2.1. Electrochemical impedance spectroscopy (EIS)

EIS is a versatile method to characterize the electrochemical systems (Barsoukov and Macdonald, 2018). When a potential perturbation of varying frequencies is applied to a battery, the impedance response can be used to evaluate several electrochemical properties. At high frequencies, the short-time processes such as capacitance and charge transfer reactions dominate the impedance. At low frequencies, the long-time processes such as diffusion in the active particles mainly contribute to the impedance. The various electrochemical properties can be obtained by fitting the impedance response using an appropriate equivalent circuit model. Since the electrochemical processes are significantly biased by the electrochemical and mechanical degradation, EIS portfolios are often utilized to characterize the battery degradation upon cycles.

To evaluate the impact of particle fracture and interfacial debonding on the battery impedance, we conduct a series of simulations to model the impedance responses. The half-cell model in Fig. 3(d) is still valid in the EIS simulation, except that the boundary condition at the current collector should be set as a potential perturbation of varying frequencies. A frequency-domain perturbation in COMSOL is used to solve the numerical equations, implying that all variables are changed

from being time dependent to frequency dependent with the following formula,

$$m = m_0 + \text{Re}\left\{ \tilde{m} \cdot e^{2\pi \xi \cdot it} \right\}, \tag{22}$$

where m is a variable which can be the voltage or current. The subscript 0 denotes the initial value around which the perturbation takes place. The tilde denotes the complex perturbation. i is the imaginary unit, ξ the frequency in Hz, and t the time. The cell impedance, Z ($\Omega \cdot m^2$), is calculated at the boundary of the cathode current collector as follows,

$$\tilde{Z} = \tilde{\phi}_{\text{app}} / \left(\mathbf{n}_{\text{cc}} \cdot \tilde{\mathbf{i}}_{\text{out}} \right) \tag{23}$$

where ϕ_{app} is the applied potential, $\mathbf{n}_{\text{cc}}$ the boundary normal vector, and $\mathbf{i}_{\text{out}}$ the output current density.

The EIS simulation is performed at the fully charged state of 4.3 V. The boundary of the cathode current collector is prescribed by a sinusoidal perturbation at the reference value 4.3 V and an amplitude of 10 mV. The model is computed for perturbation frequencies from 10 mHz to 1 kHz which is the typical range in EIS experiments (Brown et al., 2008). A capacitance C_{dl} is added at the interface between the active particles and the matrix to represent the thin double-layer formed on the surface of the active materials (Li et al., 2014). In addition, a resistance layer R_{int} is assigned at the same interface to represent the increase of the electric resistance induced by the interfacial debonding. The magnitude of the resistance R_{int} is correlated with the gap generated at the interface, which will be discussed in a later section.

3.2.2. Mechanical degradation

We model two types of mechanical degradation in the NMC electrode – particle fracture and interfacial debonding between the NMC particles and the conductive matrix. As published in our previous work (Xu et al., 2017b), the fracture of NMC secondary particles, in a form of nucleation and propagation of microcracks at the interface of the primary particles, can be modeled using a cohesive zone element. When the Li reaction induced stresses reach the strength of the cohesive elements assigned between the primary particles, intergranular cracks initiate and propagate. The damage response of the cohesive elements is presented in terms of a bilinear traction-separation relationship which is determined by two sets of parameters, namely, interfacial strength σ_{c_i} and fracture toughness G_{c_i} (Elices et al., 2002). Subscript i takes the values I and II, which represent the traction responses of stretching in the normal direction (mode I) and shear in the tangential direction (mode II), respectively. In this work, the interfacial strength and fracture toughness in the normal and shear directions are set as the same value. Interested readers may be referred to our previous work which provides in detail the modeling method and results of the intergranular fracture in NMC secondary particles (Xu and Zhao, 2018).

Interfacial debonding between the active particles and the conductive network in a composite electrode is less studied in literature. A recent work by Müller et al. used a serial connection of a dissipative damper and a spring to represent the local environment of the active particles in the porous carbon-binder matrix filled with liquid electrolyte (Müller et al., 2018). We use a similar approach but ignore the hysteresis effect induced by the dissipative damper. More specifically, a spring layer of zero thickness is prescribed at the interface. The stiffness of the spring and the debonding gap (i.e. spring extension in the normal direction) are denoted as K_{int} and λ, respectively. The interfacial debonding can be also simulated using the cohesive zone element approach, which is not used in this current work.

We consider that the interfacial resistance R_{int} is correlated with λ by the following expression,

$$R_{\text{int}} = R_{\text{int\_ref}} \cdot \left(e^{\frac{\lambda}{\lambda_{\text{ref}}}} - 1 \right), \tag{24}$$

where $R_{\text{int\_ref}}$ and λ_{ref} are defined as a reference interface resistance and a reference debonding gap, respectively. Eq. (24) defines a relationship between the interfacial resistance and the debonding gap, in which a zero debonding gap results in a zero interfacial resistance, and the interfacial resistance increases exponentially as the interfacial debonding enlarges. Consequently, when the electric contact loss occurs, the driving force for the charge transfer reaction, η, drops by a magnitude of $\Delta \eta = R_{\text{int}} \cdot i_{\text{BV}}$, which deteriorates the rate performance of batteries. Here the functional dependence of the battery impedance on the mechanical degradation at the interface is described through the two phenomenological parameters, $R_{\text{int\_ref}}$ and λ_{ref}, despite that the explicit relationship between the two quantities is unknown in existing literature.

3.3. Results and discussion

We conduct numerical modeling to understand the mechanism responsible for the spatially and temporally heterogeneous electrochemistry and mechanics in the NMC composite electrode. The half-cell is assumed to undergo a complete electrochemical cycle which starts with a galvanostatic charging and ends with a discharging with the same rate. Accordingly, we initially apply a positive current on the current collector of NMC cathode, then reverse the applied current when the battery voltage reaches the upper cutoff voltage 4.3 V, and eventually remove the current when the voltage drops to the lower cutoff voltage 3.0 V. To make a quantitative assessment on the stress effect, we will first simulate the electrochemical behaviors without considering the stress effects on Li diffusion and the surface charge transfer reaction (in Eqs. (5) and (12)), and then compare the results by considering the coupling effect. All the parameters used in the simulation are listed in the Table 1.

Fig. 5 shows the electrochemical output of NMC cycled at 5C. In a complete cycle, the half-cell voltage gradually increases up to 4.3 V from its initial open-circuit voltage around 3.0 V, and then drops back to 3.0 V after discharging, Fig. 5(a). The

Table 1
Parameters used in the theoretical modeling.

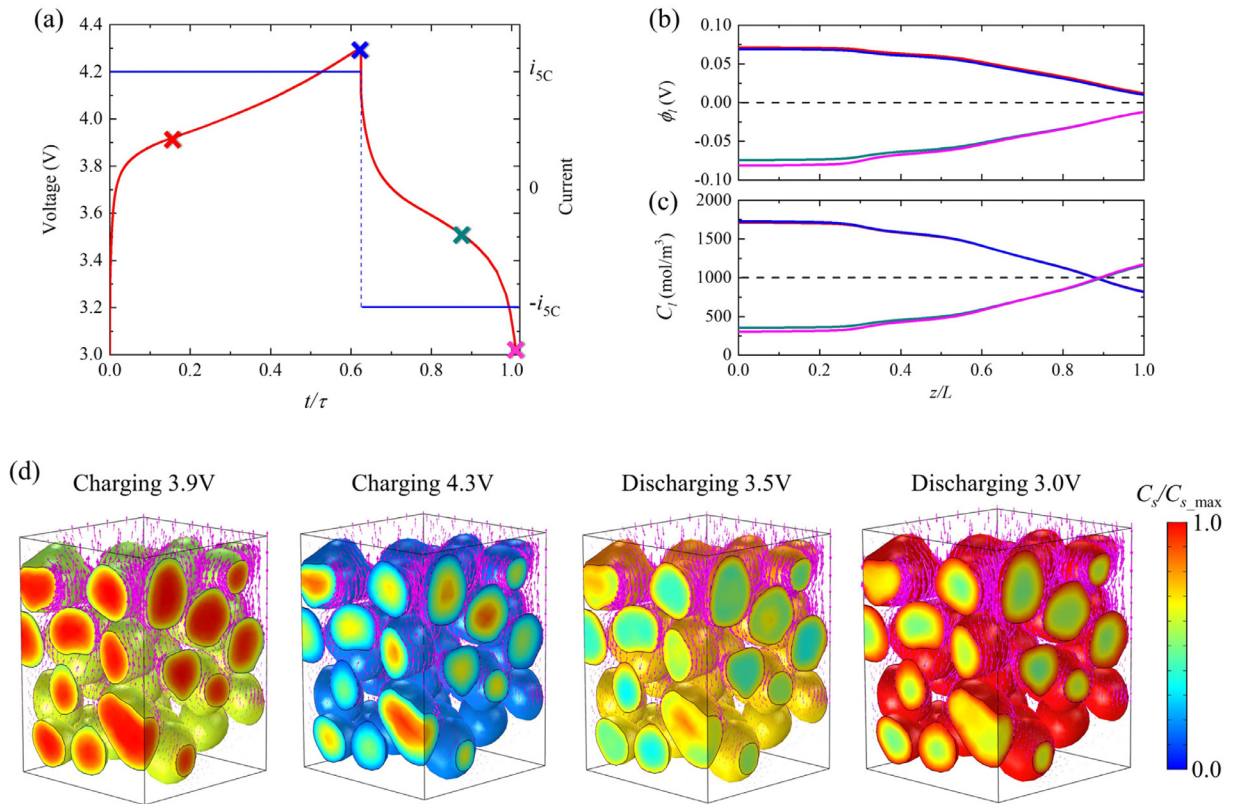| Parameter (unit)	Value	Parameter (unit)	Value
K_c (S·m^{-1})	10^4 (Hutzenlaub et al., 2014)	E_{eq} (V)	$4.4 - 2.8y + 8.2y^2 + 9.8\ y^3 - 214.5y^4 + 777.8y^5 - 1290.6y^6 + 1034.4y^7 - 324.2y^8, y = C_s/C_{s\_max}$
K_l (S·m^{-1})	1.147 (Valøen and Reimers, 2005)		
R (J·mol^{-1}·K^{-1})	8.314	L (μm)	40
T (K)	293	L_s (μm)	20
F (A·s·mol^{-1})	96,485	W (μm)	30
t_+ (l)	0.363 (Valøen and Reimers, 2005)	D_l (m^2·s^{-1})	1×10^{-10} (Valøen and Reimers, 2005)
$\partial \ln f / \partial \ln C_l$	0.43 (Hutzenlaub et al., 2014)	D_s (m^2·s^{-1})	7×10^{-15} (Cui et al., 2016)
k_c (m/s)	2×10^{-11} (Smith and Wang, 2006)	E (GPa)	140 (NMC particles); 4 (conductive matrix) (Xu et al., 2017a)
k_a (m/s)	2×10^{-11} (Smith and Wang, 2006)	υ (l)	0.3
α_c (l)	0.5 (Smith and Wang, 2006)	Ω (m^3·mol^{-1})	1.23×10^{-5}
α_a (l)	0.5 (Smith and Wang, 2006)	C_{dl} (F/m^2)	0.2 (Brown et al., 2008)
C_{s_max} (mol·m^{-3})	48,700 (Lindqvist, 2017)	G_{c_i} (J/m^2)	0.11 (Xu et al., 2017a)
C_{l_ref} (mol·m^{-3})	1	σ_{c_i} (MPa)	100
C_{l_ini} (mol·m^{-3})	1000	K_{int} (N/m^3)	1×10^{15}
i_{app} (A·m^{-2})	90 (5C)	λ_{ref} (nm)	10
ϵ_l (l)	0.5	R_{int_ref} (Ω·m^2)	2×10^{-3}

Fig. 5. Electrochemistry results of the NMC cathode cycled at 5C. (a) The applied galvanostatic current and the voltage response of the half-cell. (b)-(c) Distributions of the electrolyte voltage ϕ_l and Li concentration C_l in the electrolyte across the depth of the electrode. The colored curves in (b) and (c) correspond to the four sequential states of charge (discharge) marked in (a). (d) Li distribution C_s within NMC particles and Li flux in the electrolyte at the same four sequential states of charge. Li flux is represented by the arrows with a length proportional to the magnitude of the flux. The local Li flux near the separator (top) is significantly higher than that near the current collector (bottom), resulting in a higher utilization of the active particles near the separator. (For interpretation of the references to color in the text, the reader is referred to the web version of this article.)

x-axis in Fig. 5(a) is plotted by a normalized time t/τ, where t is the real time in Li reactions and τ the theoretical time to reach the full capacity of NMC. Under the cyclic rates of 5C, 1C, and C/5, the values of τ are 720 s, 3600 s, and 18,000 s, respectively. Assuming the battery is cycled at a very slow rate, the charging and discharging processes should in principle finish at $t/\tau = 1$ and $t/\tau = 2$, respectively. Under a fast charging rate of 5C, the active material cannot be fully utilized because of the slow kinetics of Li diffusion in the NMC particles. This results in an early termination of the charging process at $t/\tau = 0.62$ and discharging at $t/\tau = 1.02$, as shown in Fig. 5(a), which indicates that the deliverable capacity of NMC cycled at 5C is far less than its theoretical capacity.

In addition to the overall voltage response, we choose four sequential states of charge and discharge (i.e. 3.9 V, 4.3 V, 3.5 V, and 3.0 V, marked in Fig. 5(a)) to track the evolution of the electrochemical field in the NMC composite, including the electric potentials in the carbon-binder matrix ϕ_c and in the liquid electrolyte ϕ_l, as well as the Li distributions in the electrolyte C_l and in the active particles C_s. Owing to the excellent electric conductivity of carbon additive, ϕ_c exhibits a homogeneous distribution in the matrix and has the same value of the overall voltage in Fig. 5(a). Fig. 5(b) and (c) show the polarization of the liquid electrolyte potential ϕ_l and Li concentration C_l across the depth of the electrode, respectively. The *x*-axis is plotted by the normalized coordinate along the depth (i.e. *z*-direction in Fig 3(d)) of the NMC electrode where $z/L = 0$ refers to the current collector and $z/L = 1$ represents the location of the separator. Four colored curves are in correspondence to the sequential states of charge and discharge marked in Fig. 5(a). The electrolyte potential ϕ_l distributes inhomogeneously in the NMC electrode. During charging (red and blue curves), the region close to the separator shows a smaller value of ϕ_l while the region close to the current collector shows a higher ϕ_l. This depth-dependent electrolyte potential is caused by the diffusion and migration of charged species in the electrolyte. Since the Li metal on the anode side serves as a sink of Li ions during charging, the transport of Li ions induces the polarization of the electrolyte potential and results in more depletion of Li near the separator than those near the current collector, Fig. 5(c). Likewise, in the discharging process (green and pink curves) when Li migrates from Li metal to the NMC cathode, the electrolyte potential shows an opposite behavior and Li concentration near the separator is higher than that near the current collector of the cell. As discussed earlier, the electric potential ϕ_c in the conductive matrix is homogeneous throughout the entire composite, while the electrolyte potential ϕ_l exhibits a gradient along the depth of the electrode, therefore the effective electric potential $(\phi_c - \phi_l)$ exhibits a spatial variation, and the overpotential η for the charge transfer reaction at the particles/electrolyte interface, defined as $\eta = (\phi_c - \phi_l) - E_{eq}$, behaves in the same manner. In specific, the overpotential η near the separator is larger than that near the current collector during charging, contributing to a faster charge transfer rate and a higher Li flux on the particle surfaces near the separator. Fig. 5(d) plots the Li distribution C_s within NMC particles and Li flux in the electrolyte at the same four sequential states of charge and discharge shown in Fig. 5(a)–(c). Li flux is represented by the arrows with a length proportional to the magnitude of the flux. Clearly, the local Li flux near the separator (top layer) is significantly higher than that near the current collector (bottom layer), resulting in a higher Li activity in the NMC particles near the separator, which are confirmed by the contour plots of Li concentration C_s in Fig. 5(d). This spatial and temporal non-uniform utilization of the active particles generates a series of heterogeneous mechanical damage in the NMC composite as we will discuss later.

Now we explore the stress profiles in the NMC composite at the charging rate of 5C. During Li extraction, NMC experiences a volumetric contraction with the total volumetric strain being around 5%. The lattice change of NMC is proportional to the state of charge (Ryu et al., 2018). The stress field is induced by the coexisting strains, one from the eigen strain within the active particles generated by the inhomogeneous Li distribution, and the other from the mismatch strain between the active particles and the surrounding neighbor. The stress field is highly dependent on the microstructural details of the composite and is substantially different from that calculated from a freestanding particle configuration. Fig. 6(a) plots the distribution of the equivalent stress in NMC particles at the same four sequential states of charge and discharge shown in Fig. 5. During charging (Li extraction), tensile hoop stresses develop on the surface of the NMC particles due to the depletion of Li, and reach the maximum value at the charged state 4.3 V. The equivalent stress near the center of the particles is small owing to the low Li activity at a longer diffusion length under the fast charging condition. This inhomogeneous stress field promotes the nucleation and propagation of intergranular cracks between primary particles in the cycle of NMC particles as observed in Fig. 1(b). In addition to the stress inhomogeneity in the single particles, Fig. 6(a) also shows the spatial heterogeneity of the stress distribution at the composite level, which is the root of the heterogeneous mechanical damage in the NMC cathode. The stress generated in the conductive matrix is usually one or two orders of magnitude smaller than that in the active materials, partially because of the compliant nature of the carbon-binder matrix and partially because of its porous microstructure which provides free spaces to release the stress. However, the stress in the conductive matrix is not negligible which could eventually cause the fracture of the matrix and breakdown of conductive network as observed in the prior experiment (Ning et al., 2003). Fig. 6(b) plots the distribution of the equivalent stress in the conductive matrix when the cell is charged to 4.3 V. The temporal evolution is illustrated by a series of cross-sectional snapshots shown in the right panel. The stress field in the matrix shares the same feature with that in the active particles, that is, the magnitude of stresses increases as the charging proceeds while decreases in the course of discharging. It should be noted that the stress field in the porous matrix is highly dependent on the local microstructural features of the electrode such as the particle size, shape, and spacing. One common feature is that the maximum stress, red spots shown in Fig. 6(b), is always located at the narrow regimes where NMC particles are close and aging of the matrix is most likely to occur.

The mechanical stress in batteries influences the diffusion kinetics and the charge transfer reaction. We evaluate the stress effects separately to make a quantitative comparison. We first include the stress term in Eq. (5) in the numerical modeling to evaluate the effect of the stress-assisted diffusion on the battery performance. Fig. 7(a) plots the comparison
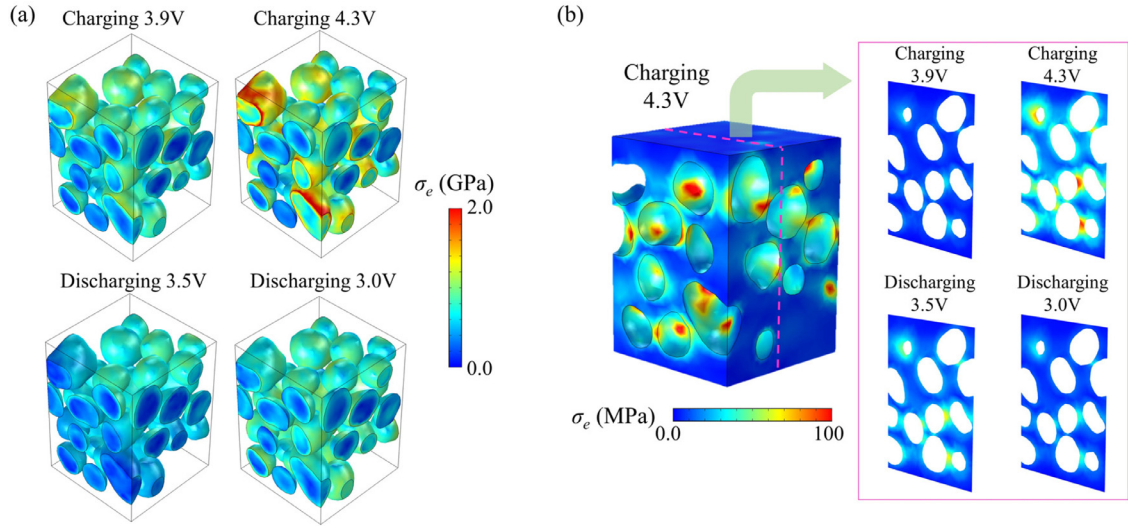
Fig. 6. Stress profiles in the NMC electrode cycled at 5C. The snapshots correspond to the same four sequential states of charge in Fig. 5. (a) and (b) show the distributions of the equivalent stress in NMC particles and in the conductive matrix, respectively. Stresses are generated as a result of Li transport and the mechanical interaction between the active particles and the conductive matrix. The stress profiles depend on the local microstructural detail of the model. (For interpretation of the references to color in the text, the reader is referred to the web version of this article.)
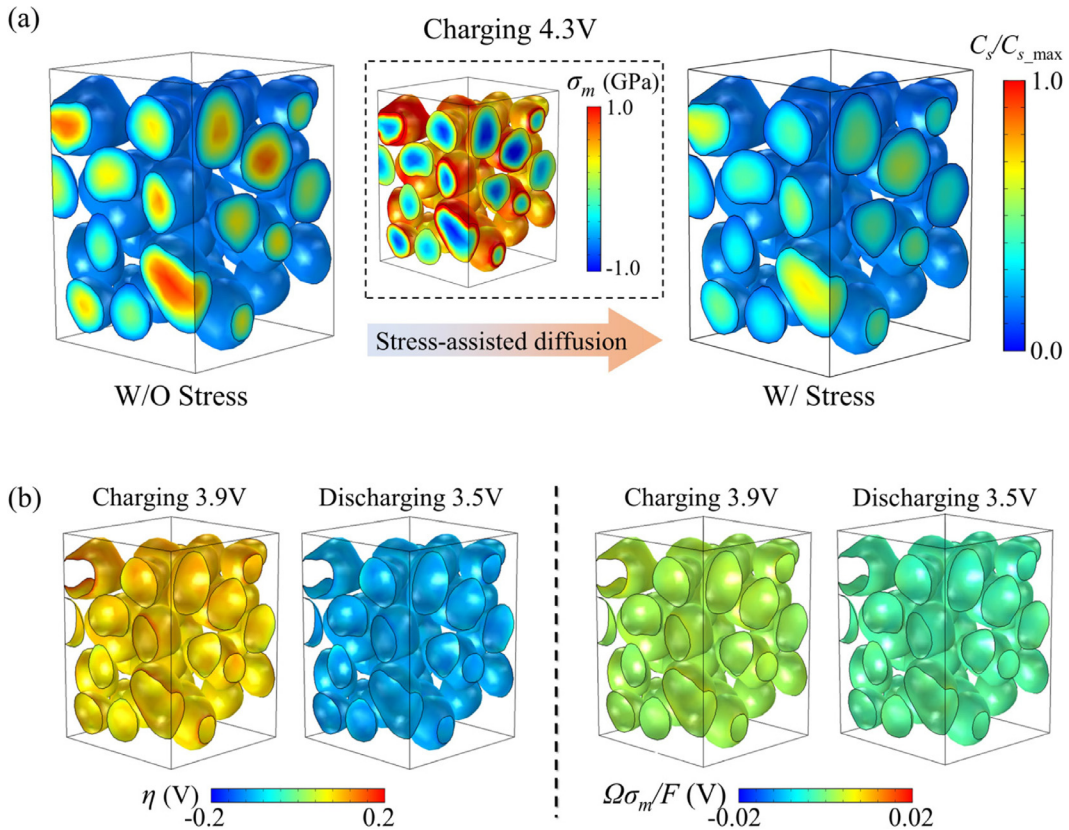
Fig. 7. Evidence of stress-regulated Li diffusion and stress-biased overpotential. (a) The comparison of Li distribution in NMC particles at the fully charged state with and without considering the stress effect. Inset shows the mean stress profile at the same charged state. The stress gradient drives Li diffusion from the compressed regime (near the core) to the tensed regime (near the surface) during charging, thereby increasing the Li activity at the center of NMC particles. (b) The electrochemical overpotential η (left) and stress-biased voltage $\Omega\sigma_m/F$ (right) are mapped on the NMC particle surfaces at the charged (3.9 V) and discharged (3.5 V) states.
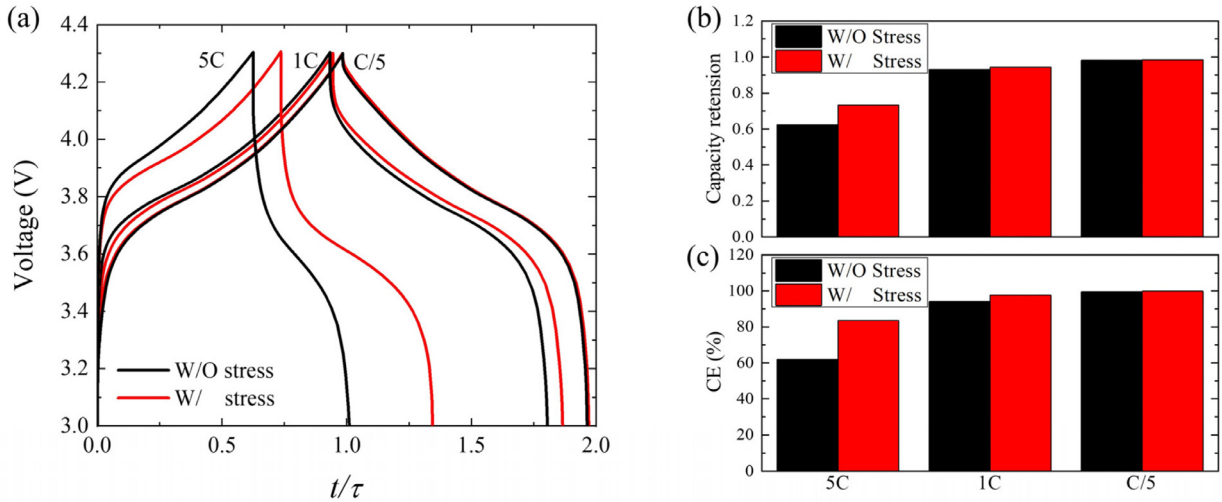
Fig. 8. The impact of mechanical stresses on the electrochemical performance of the half cell in terms of the (a) voltage response, (b) capacity retention, and (c) coulombic efficiency (CE) of the battery cycled at three different rates. The influence originates from the stress-regulated Li diffusion in the NMC particles as well as the stress-biased charge transfer at the interface between the electrode and the electrolyte. The coupling effect is magnified at the fast charging condition. (For interpretation of the references to color in the text, the reader is referred to the web version of this article.)

of Li distribution in NMC particles at the fully charged state with and without considering the stress effect. Li distribution within the NMC particles is more homogeneous when the stress effect is included. This difference is attributed to the effect of the stress gradient on Li diffusion. During charging, Li ions diffuse out from the NMC particles. As discussed earlier, the outer shell of NMC particles is under tension while the interior of the particles is compressed. The inset of Fig. 7(a) shows the profile of the hydrostatic stress. Li diffusion is driven by both the gradient of Li concentration and the gradient of stresses. Therefore, the stress gradient enhances the outward Li diffusion from the NMC particles, facilitating the fast charging process and improving the Li activity in the electrode.

Stress also modifies the overpotential across the interface between the electrolyte and the active species, and thus biases the rate of charge transfer at the interface. In the writing of the overpotential, $\eta = \phi_c - \phi_l - E_{eq} - \Omega\sigma_h/F$, a tensile hydrostatic stress decreases the overpotential for the charge transfer reaction. When the surface of the NMC particles is subject to a tensile stress during charging, the stress field would retard the charging process and minimize the deliverable capacity at a given time window. This is an opposite effect compared to the stress-mediated diffusion. Here we make a comparison between the electrochemical overpotential and the stress-biased overpotential in Fig. 7(b), which shows the distribution of η (left) and the stress-biased voltage $\Omega\sigma_m/F$ (right) on the surface of NMC particles at the charged (3.9 V) and discharged (3.5 V) states. We find that the stress-biased voltage is in the range of 0–±10 mV, which is one order of magnitude smaller than the overall overpotential (0–±200 mV). This concludes that the stress effect on charge transfer reaction may not be significant relative to the electrochemical driving force. Therefore, the stress effect on the capacity and potential of batteries mainly comes from the stress-regulated bulk diffusion.

Now we evaluate the impact of the stress on the battery performance by accounting for the stress effects on both diffusion and charge transfer. Fig. 8 (a–c) plot the voltage response, capacity retention, and coulombic efficiency (CE) of the half-cell in a complete cycle at three different rates C/5, 1C, and 5C. The capacity retention at different charging rates is calculated by the capacity of the half-cell at the time of the cut-off voltage divided by the theoretical capacity. The coulombic efficiency is defined as the ratio of the available discharge capacity to the overall charge capacity. The results marked by the black and red colors are obtained separately from the simulations without and with considering the stress effects. While the voltage response shows the similar feature in the two cases, Fig. 8(a), the deliverable capacity at both the fully charged and discharged states is much improved by the stress-assisted Li transport in the NMC particles. This coupling effect is magnified at the fast charging condition (i.e. 5C), indicating a positive influence of the stress on the rate performance of batteries. Moreover, Fig. 8 (b–c) demonstrate that the capacity retention and coulombic efficiency of the cell under the fast charging condition are largely enhanced by the back stress effect.

Moving away from the assessment of the impact of stresses on the kinetics of Li transport and the thermodynamics of charge transfer, we model the various types of mechanical damage as we observed in Figs. 1 and 2. Particle fracture is one of the major mechanical degradation. In Fig. 2(a), the X-ray tomography data has displayed a clear depth-dependent pattern of particle fracture in the NMC composite. Numerical modeling provides mechanistic understanding of this spatial heterogeneity of mechanical failure. As discussed earlier, Li extraction from NMC during charging generates a field of tensile hoop stress near the particle surface and compressive stress near the center. The tensile stress drives the initiation and propagation of intergranular cracks between the primary particles. Fig. 9(a) shows the equivalent stress profile in NMC particles at the charged state of 3.9 V. It is evident that the stress distribution on particle surfaces is highly inhomogeneous
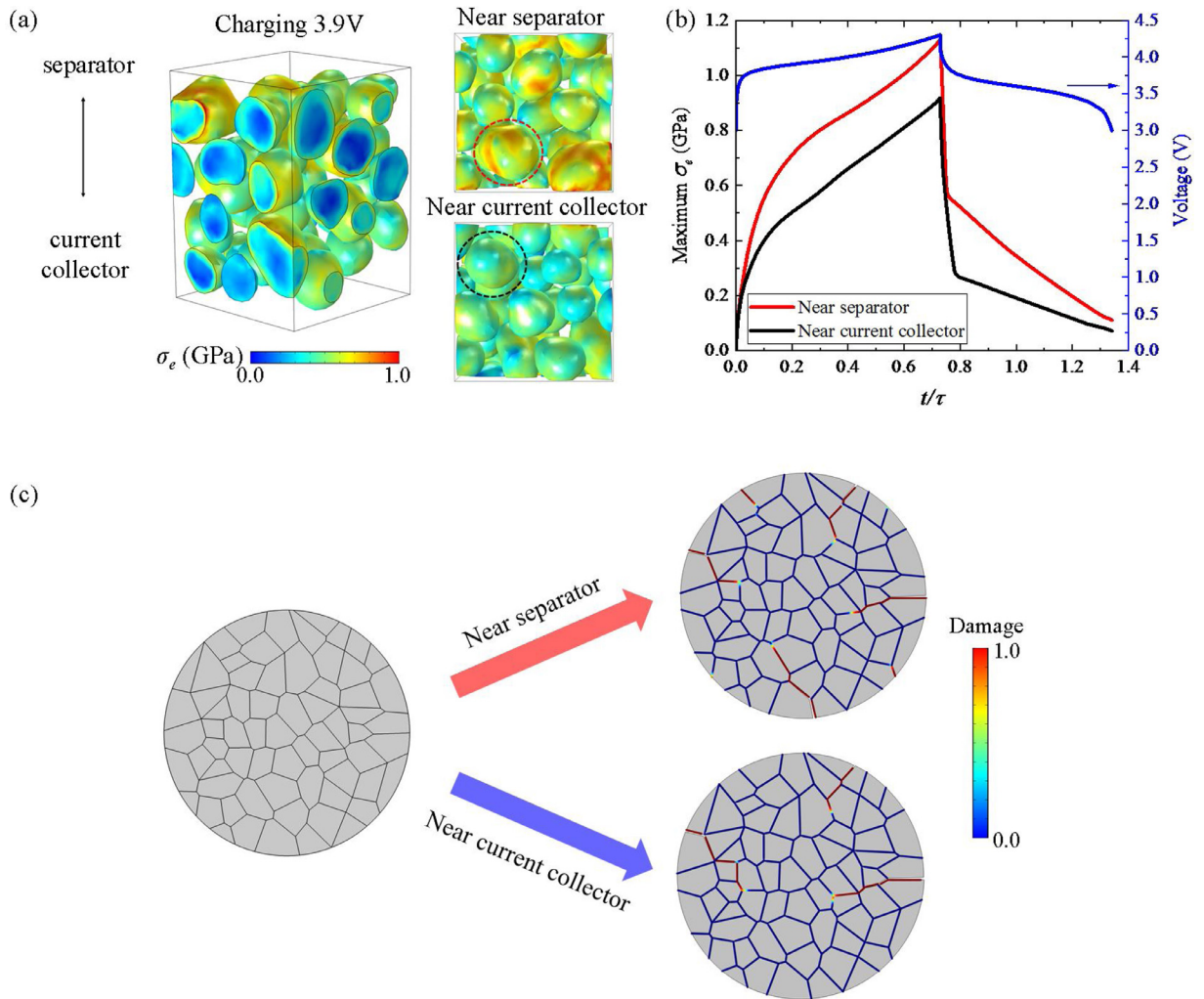
Fig. 9. The spatial heterogeneity of stresses in the NMC composite. (a) The equivalent stress profile in NMC particles at a charged state (3.9 V). NMC particles near the separator develop a much higher stress field because of the deeper charge (discharge) states as described in Fig. 5. (b) shows the time evolution of the maximum equivalent stress in a NMC particle near the separator (marked by a red dashed circle in (a)) and in a particle near the current collector (see the black dashed circle in (a)). (c) The stress field is used to model the intergranular fracture in NMC secondary particles. A 2D model of a spherical NMC secondary particle consisting of irregular primary particles is built. The crack patterns in the particles at the two locations are compared using a damage variable where 1 represents the damaged interface and 0 represents the pristine interface. The particle near the separator shows more severe intergranular fracture. (For interpretation of the references to color in the text, the reader is referred to the web version of this article.)

even within a single particle. The regimes with a higher stress will be more likely to experience intergranular cracks, which will in turn synergistically results in localized heterogeneous electrochemical behaviors. Looking at the composite electrode in the depth direction, higher stresses develop in the NMC particles near the separator (the upper layer) than the particles near the current collector (the lower layer), because of the depth-dependent Li activity as discussed in Fig. 5. To make a quantitative comparison at the two locations, we select two local particles with similar size and shape, and plot the temporal evolution of the maximum equivalent stress for these two particles in Fig. 9(b). For the most time during charging, the particle near the separator (marked by a red dashed circle in Fig. 9(a)) is subject to a stress about 30% higher than that in the particle near the current collector (the black dashed circle). Such a depth-dependent stress field will ultimately induce the spatial heterogeneity of particle fracture in the NMC electrode. To illustrate the initiation and propagation of intergranular cracks in the two particles in NMC, we generate a simplified 2D model of a spherical NMC secondary particle consisting of multiple irregular primary particles using the Voronoi tessellation. Every primary particle within the model has its random grain orientations and experiences an anisotropic strain upon Li reactions. We set the strains in the a- and b-axis to be -2% (lattice contraction), and in the c-axis to be 1% (lattice expansion) during Li extraction, according to a prior study of the Bragg peak shifting in in-situ XRD scanning experiments (Ryu et al., 2018). The magnitude of the anisotropic strain is assumed to be proportional to the Li concentration. We extract the averaged surface Li flux on those two particles in the reconstructed model (Fig. 9(a)), and apply the flux as a boundary condition to the simplified model. The local Li flux near the

Table 2
Fitted EIS parameters for the models with and without the interfacial debonding.

	R_Ω ($\Omega \cdot m^2$)	R_{ct} ($\Omega \cdot m^2$)	C_{dl} (F/m^2)	Z_w ($\Omega \cdot m^2/s^{1/2}$)
Without interfacial debonding	0.000779	0.00673	0.783	0.00109
With interfacial debonding	0.0279	0.0230	0.159	0.00225

separator is much higher than that toward the bottom of the current collector, thereby inducing a deeper charge (discharge) and thus a larger stress field. The dynamics of intergranular fracture is simulated using a cohesive zone model (Xu and Zhao, 2018). The snapshots in Fig. 9(c) shows the intensity of the intergranular cracks in the two particles using a damage variable, where 1 represents the fully detached interface and 0 represents the pristine interface. Clearly, the NMC secondary particle near the separator experiences more structural decohesion at the grain boundaries which is in excellent agreement with our experimental results. The heterogeneous mechanical damage originates from the polarization of the electric field and various Li activities along the thickness of the composite electrode. Modeling the intergranular fracture in NMC is not the major focus of this paper since we have systematically studied this phenomenon by incorporating its nature of corrosive fracture in a recent publication (Xu and Zhao, 2018). We have also studied the influence of the particle decohesion in NMC on the battery performance (Xu et al., 2017b). We have shown that the electrochemical impedance significantly increases upon particle fracture because the formation of extra SEI on the surface of fractured secondary particles impedes both electronic and ionic conduction through the SEI. Furthermore, fracture increases the surface area of the irreversible side reactions and contributes to the steady fade of the cyclic efficiency.

Mechanical failure at the interface between the active particles and the inactive matrix is another important mechanism of aging in batteries but is relatively less studied. In addition to the full-field X-ray tomographic characterization, we use FIB/SEM to create a refined cross-section of NMC cathode to visualize the interfacial debonding. Fig. 10(a) shows the cross-sectional images before and after electrochemical cycles. The incurred interfacial debonding between the NMC particles and the conductive matrix is outlined by the yellow dashed lines in the cycled sample. The loss of interfacial contact is a consequence of the mismatch strain between the NMC particles and the matrix. Our goal here is to quantify the electrochemical performance of batteries, in terms of the impedance, the voltage response, and capacity, influenced by the mechanical degradation at the interface using the fully coupled model. On one side, the cyclic Li reaction generates a field of stress in the composite including the NMC particles, the conductive matrix, and the interfaces. On the other side, the interfacial failure facilitates the loss of electric contact and dramatically reduces the metrics of battery performance. Fig. 10(b) shows the Li profile at the fully charged state of 4.3 V. The cross section of the NMC electrode is color coded by the Li concentration C_s/C_{s_max} in the particle regime and C_l/C_{l_ini} in the electrolyte regime. Arrows represent the local Li flux in the electrolyte. During charging, the mismatch strain at the particle/electrolyte interfaces generates the mechanical debonding which is magnified by the gaps in Fig. 10(b). Meanwhile, the interfacial resistance R_{int} significantly increases as the gap develops which retards the electron transport to the redox site on the particle surfaces. The driving force for the charge transfer reaction, η, drops by a magnitude of $\Delta\eta = R_{int} \cdot i_{BV}$. One obvious consequence is the deterioration of the rate performance of batteries. Another effect is the evolved inhomogeneous Li distribution on the particle surfaces – the detached regimes of NMC particles (marked by the red circles) undergo a much slower charging (Li extraction) and thus contain more residual Li than the well-bonded regimes.

To quantify the influence of the interfacial damage on the cell performance, we conduct numerical modeling of EIS experiments. The Nyquist plot, a complex plot of the electrochemical impedance for a battery stimulated by a perturbation of varying frequencies, is commonly used to quantify the transport properties for the short-term or long-term processes. Fig. 10(c) shows the Nyquist plots (solid lines) simulated with and without considering the interfacial debonding in the model. All the Nyquist plots show a typical semicircle at the high frequency domain which is attributed to the charge transfer reactions, and a Warburg tail at low frequency which is due to the Li diffusion in the active particles (Zhang et al., 2006). The transport properties for different electrochemical processes can be extracted from the Nyquist plots using an equivalent circuit model. The dashed lines represent the fitting curves using a circuit model shown in the inset of Fig. 10(c), where R_Ω represents the electric ohmic resistance from the electrolyte, the carbon-binder matrix, and the interface between the active and inactive materials, R_{ct} the resistance for the surface charge transfer, C_{dl} the capacitance for the electric double layer, and Z_w the Warburg impedance for Li diffusion in the bulk active material. Table 2 summarizes the fitted impedance parameters for the models with and without considering the interfacial debonding. As shown in Table 2, both R_Ω and R_{ct} significantly increase when the interfacial debonding occurs. The loss of contact of the active materials to the conductive agents impedes electron transport and the charge transfer reaction. Ultimately, this interfacial degradation results in a high polarization and significant capacity loss in batteries as demonstrated in the voltage plots in Fig. 10(d).

As shown in the experimental tomography in Fig. 2, the interfacial debonding exhibits a heterogeneous pattern that NMC particles near the separator tend to be detached from the conductive network more severely in the early cycle. Here we use computational modeling to simulate the dynamics of the interfacial debonding in the 3D space. In Fig. 11(a), the interfaces between the active particles and the matrix are color coded by the calculated interfacial gap λ at the charged state of 4.3 V. The degree of interfacial damage is correlated with the depth-dependent states of charge and stresses as we discussed in Figs. 5 and 9. The particles near the separator are more utilized in the Li reactions and thus experience a higher mismatch
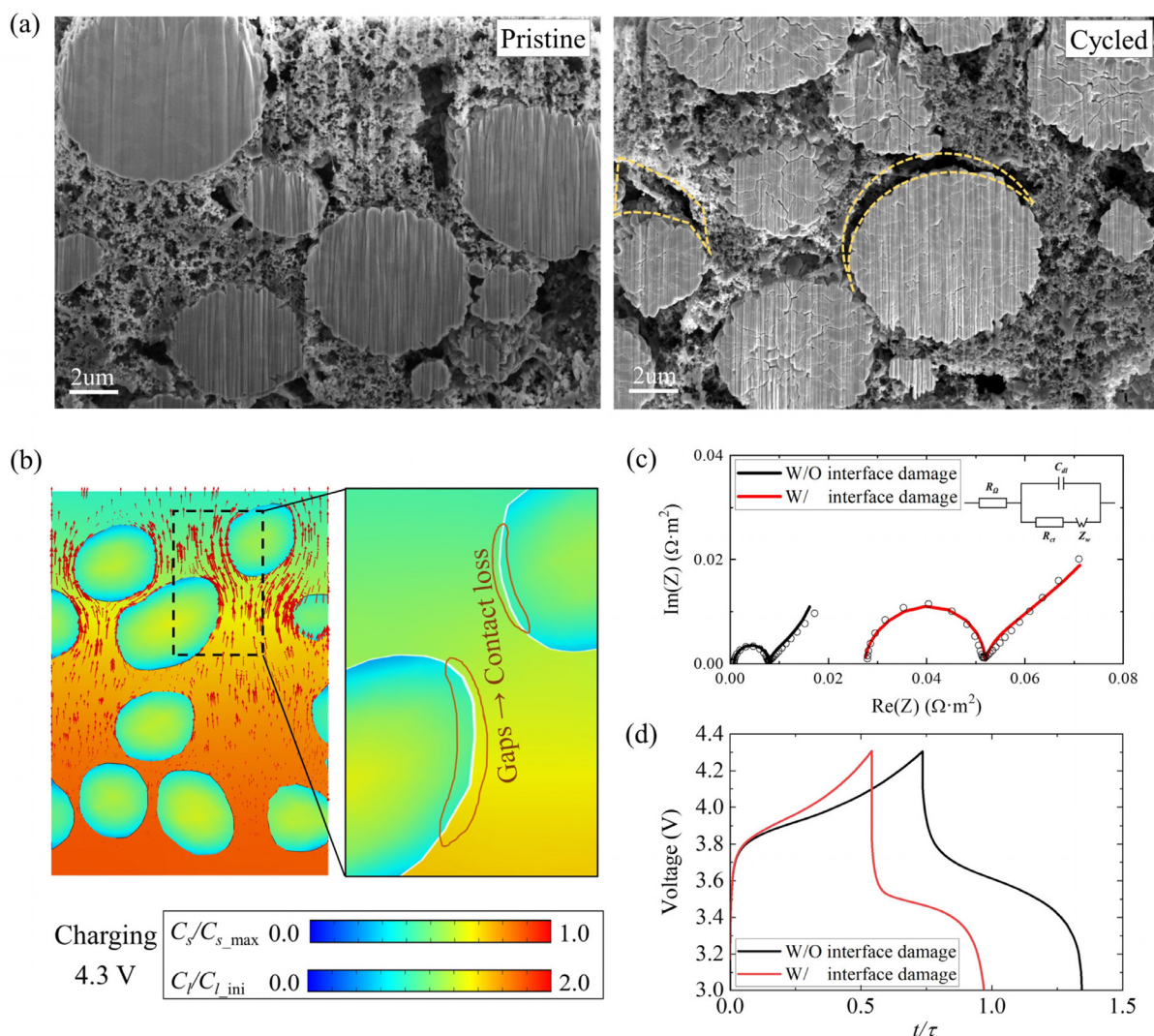
Fig. 10. Experiments and modeling of interfacial debonding in NMC composite cathode. (a) Cross-sectional images of NMC before and after cycles. The incurred interfacial debonding between the NMC particles and the conductive matrix are outlined by the yellow dashed lines in the cycled sample. (b) Computational modeling of the electrochemical behavior of NMC influenced by the interfacial debonding. The cross section is color coded by the Li concentration C_s/C_{s_max} in the particle regime and C_l/C_{l_ini} in the electrolyte regime. Arrows represent the local Li flux in the electrolyte. The gaps at the interfaces are shown in the enlarged image. (c) The Nyquist plots (solid lines) simulated with and without considering the interfacial debonding in the model. The electrochemical impedance can be extracted from the Nyquist plots using an equivalent circuit model. The interfacial contact loss induces high polarization and significant capacity loss in batteries as evident in the voltage plots in (d). (For interpretation of the references to color in this figure legend, the reader is referred to the web version of this article.)

strain with the conductive matrix. Therefore, more localized interfacial debonding develops near the separator. The higher probability of interfacial damage would deactivate the NMC particles near the separator by isolating the particles from the conductive network. Consequently, the less damaged particles toward the current collector take part in more electrochemical activities in the later cycles, making the heterogeneous particle fracture and interfacial debonding a quite dynamic process over cycles. Mechanical damage in the composite electrode is indeed an evolving heterogeneous field depending on the position and time. Fig. 11(b) explores the role of the microstructural details in the development of interfacial failure. Three exemplary particles are selected to show the spatial heterogeneity. The interfacial debonding is a complex field even for a single particle. The interface between two close particles tends to experience more severe damage due to the mismatch strain caused by the concurrent contraction of the two particles. The interfacial condition regulates the rates of electron transport and charge transfer. The detached regimes of NMC particles undergo a slower charging and discharging cycle than the well-bonded regimes, which catalyzes a more inhomogeneous field of Li concentration and stresses (Fig. 11(c)) and facilitates more heterogeneous electrochemistry and mechanical failure.

There is no question about the influence of mechanical failure on the downgrading of the electrochemical metrics. This relationship is a piece of important information missing in the current study of the field. Our last task here is to perform
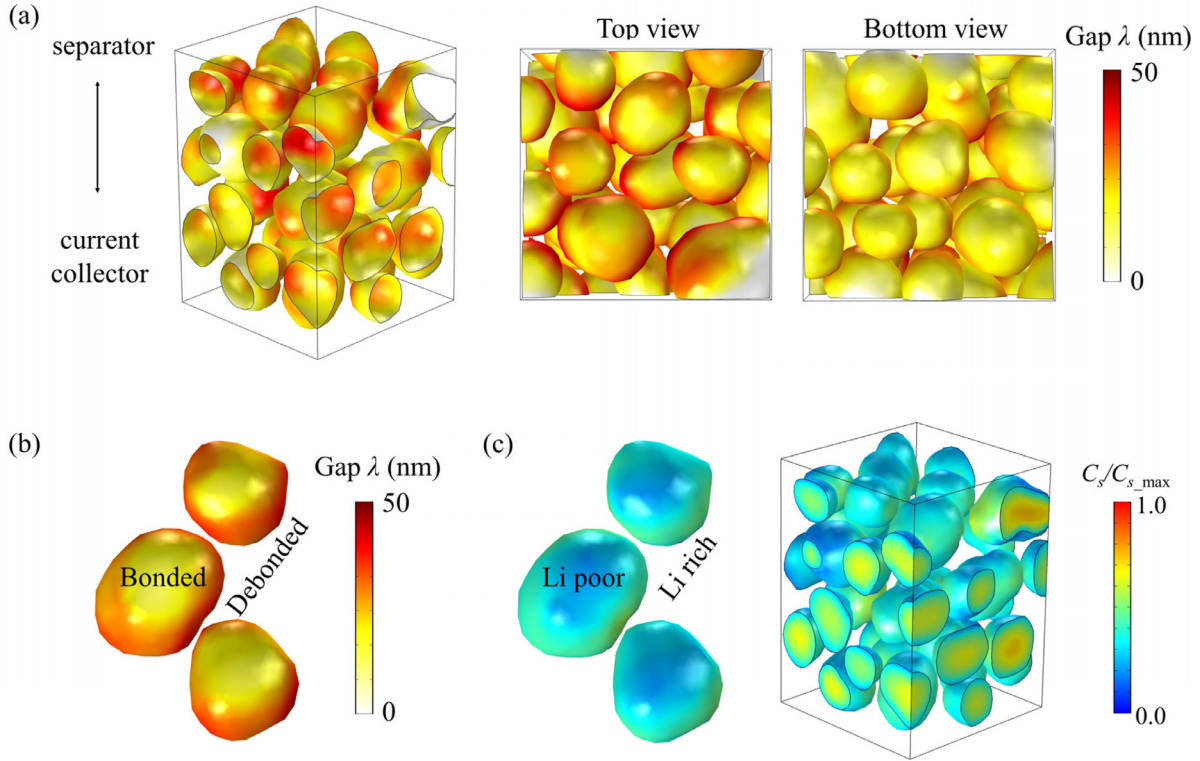
Fig. 11. The spatial heterogeneity of interfacial debonding in the NMC cathode. (a) The composite at the fully charged state is color coded by the calculated interfacial gap between the NMC particles and the conductive matrix. The degree of interfacial damage is correlated with the depth-dependent states of charge as discussed in Figs. 5 and 9. (b) For the three exemplary given particles, the local interfacial debonding is highly dependent on the local microstructural detail – the interface between two close particles tends to experience more severe damage. (c) Interfacial debonding impedes electron transport and surface charge transfer, resulting a more inhomogeneous field of Li concentration. The well-bonded NMC particles undergo more Li cycles than those detached particles – in the extreme case that the NMC particles are isolated from the conductive network, the particles become inactive to Li reactions. (For interpretation of the references to color in this figure legend, the reader is referred to the web version of this article.)

Table 3
Fitted EIS parameters for the models with different K_{int}.

K_{int} (N/m^3)	R_{Ω} ($\Omega \cdot$m^2)	R_{ct} ($\Omega \cdot$m^2)	C_{dl} (F/m^2)	Z_w ($\Omega \cdot$m^2/s$^{1/2}$)
5×10^{14}	0.0579	0.0336	0.0973	0.00278
1×10^{15}	0.0279	0.0230	0.159	0.00225
2×10^{15}	0.00245	0.00888	0.544	0.00136

a parametric study on the correlation between the interfacial damage and the electrochemical performance since most of the interfacial properties are unknown. We first examine the effect of the interfacial stiffness K_{int}. Fig. 12(a) plots the relationships between the interfacial tension and the gap for three different interfacial stiffness, $K_{int} = 5 \times 10^{14}$, 1×10^{15}, and 2×10^{15} N/m^3, respectively. A smaller value of the interfacial stiffness gives a larger interfacial gap λ at a given stress. Here we fix the dependence of the interface resistance R_{int} on λ (blue line) using an exponential function in Eq. (24) and set $\lambda_{ref} = 10$ nm and $R_{int\_ref} = 2 \times 10^{-3}$ $\Omega \cdot$m^2. Fig. 12(b) and (c) show the EIS profile and the voltage response of batteries with the three different interfacial stiffness. The solid, dashed, and dotted lines correspond to the three values $K_{int} = 5 \times 10^{14}$, 1×10^{15}, and 2×10^{15} N/m^3, respectively. The fitted EIS parameters for the models of different K_{int} in Fig. 12(b) are listed in Table 3. As expected, both R_{Ω} and R_{ct} significantly increase as the interfacial stiffness decreases. Such a high impedance induces significant capacity loss and polarization in batteries as shown in the voltage plots in Fig. 12(c). Next, we use a similar approach to evaluate the electrochemical performance when different relationships between the interfacial resistance R_{int} and the interfacial gap λ are defined. Fig. 12(d) plots three different functions ($R_{int\_ref} = 2 \times 10^{-5}$, 2×10^{-4}, and 2×10^{-3} $\Omega \cdot$m^2) between R_{int} and λ. The interfacial stiffness is fixed as 1×10^{15} N/m^3. Fig. 12(e) and (f) plot the electrochemical impedance and the voltage profile, respectively, under the assumption of the three different functions. A higher value of R_{int_ref}, representing more sensitivity of the interfacial resistance on the physical gap, causes more increase of the impedance (Table 4), and thus more potential polarization and capacity loss (Fig. 12(f)). In brief, improving the mechanical stability and the electric conductivity at the interface between the active species and the inactive agents are crucial to
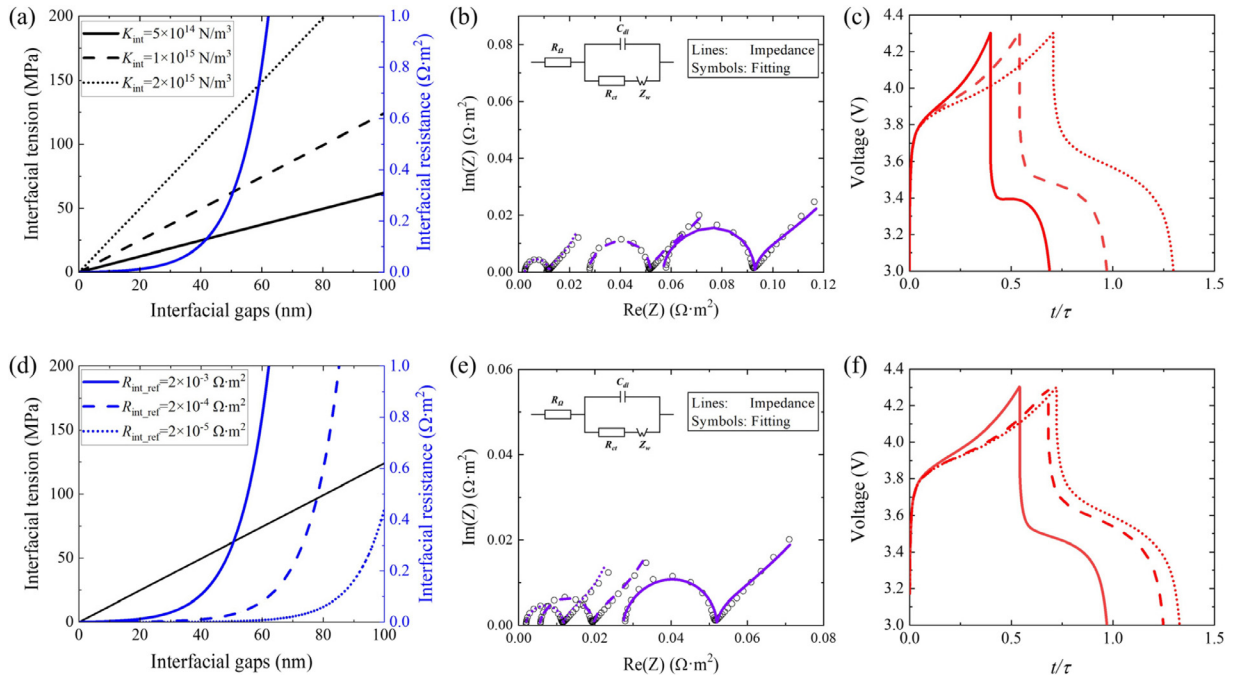
Fig. 12. Parametric studies on the correlation between the interfacial damage and the electrochemical performance. (a) Three different interfacial stiffness ($K_{int} = 5 \times 10^{14}$, 1×10^{15}, and 2×10^{15} N/m³) are utilized to analyze the effect of the interfacial strength on the electrochemical impedance (b) and the voltage profile (c). (d) Three different functions ($R_{int\_ref} = 2 \times 10^{-5}$, 2×10^{-4}, and 2×10^{-3} Ω·m²) between the resistance and the interfacial gap are used to analyze the effect of R_{int_ref} on the electrochemical impedance (e) and the voltage profile (f). (For interpretation of the references to color in the text, the reader is referred to the web version of this article.)

Table 4
Fitted EIS parameters for the models with different R_{int_ref}.

R_{int_ref} (Ω·m²)	R_Ω (Ω·m²)	R_{ct} (Ω·m²)	C_{dl} (F/m²)	Z_w (Ω·m²/s$^{1/2}$)
2×10^{-5}	0.00192	0.00923	0.513	0.00139
2×10^{-4}	0.00570	0.0131	0.310	0.00165
2×10^{-3}	0.0279	0.0230	0.159	0.00225

maintain the battery performance over cycles. This is apparently more of significance for the solid-state batteries where the poor mechanical compatibility and the high resistance at the solid-solid interface are the critical challenges for the current techniques.

4. Conclusions

This work combines the merits of the advanced synchrotron X-ray tomography analysis and the microstructure-resolved computational modeling to study the heterogeneous electrochemistry and mechanics in a composite cathode in commercial batteries. We focus on the spatially and temporally evolving heterogeneous damage from the macroscopic level of composites down to the single particles.

Rely on the recently developed X-ray nano-tomography and transmission techniques, the morphological defects in an NMC cathode can be visualized at multi-scales. Particle fracture and interfacial debonding are identified in a large set of tomographic data for over a thousand of NMC particles. The mechanical degradation shows a depth-dependent pattern. The degree of particle fracture in NMC particles is much higher in the region near the separator than toward the current collector. The interfacial debonding shows a similar distribution that the particles near the separator tend to be more separated from the conductive network.

We use theoretical modeling to provide mechanistic understanding of the heterogeneous damage in batteries. We develop a finite element program based on the fully coupled electro-chemo-mechanics theory. We apply the method to a statistically validated model to simulate the fields of electrochemistry and mechanics in the NMC cathode upon Li reactions. We calculate the evolving Li distribution and mechanical stresses in the 3D space for a complete cycle of charging and discharging. At the particle level, the inhomogeneous Li distribution within single NMC particles induces a field of mechanical stresses. The developed stress regulates the kinetic of Li diffusion and the thermodynamics of charge transfer. We evaluate that the stress-assisted diffusion is a major factor that influences the voltage profile, capacity, and cyclic efficiency in bat-

teries. At the electrode level, the particles near the separator experience deeper charge and discharge over cycles and thus are subject to a larger stress. The difference in the Li activity originates from the polarization of the electrolyte potential and the non-uniform distribution of the activation energy for the charge transfer reaction. The stress profile in the NMC composite causes a spatial heterogeneity of mechanical degradation as we observed in experiments. We model the initiation and propagation of intergranular cracks in the secondary particles at different locations. The fracture pattern provides a clear evidence that the various Li activities in NMC particles are the major cause of the heterogeneous fracture in NMC. A similar conclusion is obtained in the modeling of interfacial debonding between the active particles and the conductive matrix. The spatially heterogeneous interfacial failure could reconstruct the conductive network and redistribute the electrochemical activities of NMC particles in the electrode, highlighting a dynamic nature of electrochemistry and mechanics evolving over time in the composite electrode. We further quantify the influence of the mechanical damage on the metrics of battery performance. We simulate the electrochemical impedance profile to build a relationship between the interfacial debonding and the impedance of electron transport and surface charge transfer. The interfacial damage impedes the electron conduction and results in significant capacity loss and polarization in batteries.

Acknowledgments

Reference

Anand, L., 2012. A Cahn-Hilliard-type theory for species diffusion coupled with large elastic-plastic deformations. J. Mech. Phys. Solids 60, 1983–2002.

Armand, M., Tarascon, J.-M., 2008. Building better batteries. Nature 451, 652.

Bak, S.-M., Shadike, Z., Lin, R., Yu, X., Yang, X.-Q., 2018. In situ/operando synchrotron-based X-ray techniques for lithium-ion battery research. NPG Asia Mater. 10, 563–580.

Barsoukov, E., Macdonald, J.R., 2018. Impedance Spectroscopy: Theory, Experiment, and Applications, third ed. John Wiley & Sons.

Besnard, N., Etiemble, A., Douillard, T., Dubrunfaut, O., Tran-Van, P., Gautier, L., Franger, S., Badot, J.-C., Maire, E., Lestriez, B., 2017. Multiscale morphological and electrical characterization of charge transport limitations to the power performance of positive electrode blends for lithium-ion batteries. Adv. Energy Mater. 7, 1602239.

Bower, A.F., Guduru, P.R., Sethuraman, V.A., 2011. A finite strain model of stress, diffusion, plastic flow, and electrochemical reactions in a lithium-ion half-cell. J. Mech. Phys. Solids 59, 804–828.

Brassart, L., Suo, Z., 2013. Reactive flow in solids. J. Mech. Phys. Solids 61, 61–77.

Brown, S., Mellgren, N., Vynnycky, M., Lindbergh, G., 2008. Impedance as a tool for investigating aging in lithium-ion porous electrodes: II. Positive electrode examination. J. Electrochem. Soc. 155, A320–A338.

Canny, J., 1987. A computational approach to edge detection. In: Fischler, M.A., Firschein, O. (Eds.), Readings in Computer Vision. Morgan Kaufmann, San FranciscoCA, pp. 184–203.

Cesar da Silva, J., Pacureanu, A., Yang, Y., Bohic, S., Morawe, C., Barrett, R., Cloetens, P., 2017. Efficient concentration of high-energy X-rays for diffraction-limited imaging resolution. Optica 4, 492–495.

Christensen, J., Newman, J., 2006. Stress generation and fracture in lithium insertion materials. J. Solid State Electrochem. 10, 293–319.

Chung, M., Seo, J., Zhang, X., Sastry, A., 2011. Implementing realistic geometry and measured diffusion coefficients into single particle electrode modeling based on experiments with single $LiMn_2O_4$ spinel particles. J. Electrochem. Soc. 158, A371–A378.

Cloetens, P., Ludwig, W., Baruchel, J., Dyck, D.V., Landuyt, J.V., Guigay, J.P., Schlenker, M., 1999. Holotomography: Quantitative phase tomography with micrometer resolution using hard synchrotron radiation X rays. Appl. Phys. Lett. 75, 2912–2914.

Cui, S., Wei, Y., Liu, T., Deng, W., Hu, Z., Su, Y., Li, H., Li, M., Guo, H., Duan, Y., Wang, W., Rao, M., Zheng, J., Wang, X., Pan, F., 2016. Optimized temperature effect of Li-ion diffusion with layer distance in $Li(Ni_xMn_yCo_z)O_2$ cathode materials for high performance Li-ion battery. Adv. Energy Mater. 6, 1501309.

Dolotko, O., Senyshyn, A., Mühlbauer, M.J., Nikolowski, K., Ehrenberg, H., 2014. Understanding structural changes in NMC Li-ion cells by in situ neutron diffraction. J. Power Sources 255, 197–203.

Doyle, M., Fuller, T.F., Newman, J., 1993. Modeling of galvanostatic charge and discharge of the lithium/polymer/insertion cell. J. Electrochem. Soc. 140, 1526–1533.

Ebner, M., Geldmacher, F., Marone, F., Stampanoni, M., Wood, V., 2013a. X-ray tomography of porous, transition metal oxide based lithium ion battery electrodes. Adv. Energy Mater. 3, 845–850.

Ebner, M., Marone, F., Stampanoni, M., Wood, V., 2013b. Visualization and quantification of electrochemical and mechanical degradation in Li ion batteries. Science 342, 716–720.

Elices, M., Guinea, G.V., Gomez, J., Planas, J., 2002. The cohesive zone model: advantages, limitations and challenges. Eng. Fract. Mech. 69, 137–163.

Fuller, T.F., Doyle, M., Newman, J., 1994. Simulation and optimization of the dual lithium ion insertion cell. J. Electrochem. Soc. 141, 1–10.

Hao, X., Lin, X., Lu, W., Bartlett, B.M., 2014. Oxygen vacancies lead to loss of domain order, particle fracture, and rapid capacity fade in lithium manganospinel ($LiMn_2O_4$) batteries. ACS Appl. Mater. Interfaces 6, 10849–10857.

Huggins, R.A., Nix, W.D., 2000. Decrepitation model for capacity loss during cycling of alloys in rechargeable electrochemical systems. Ionics (Kiel) 6, 57–63.

Hun, J., Chung, M., Park, M., Woo, S., Zhang, X., Marie, A., 2011. Generation of realistic particle structures and simulations of internal stress: A numerical/AFM study of LiMn2O4 particles. J. Electrochem. Soc. 158, A434–A442.

Hutzenlaub, T., Thiele, S., Paust, N., Spotnitz, R., Zengerle, R., Walchshofer, C., 2014. Three-dimensional electrochemical Li-ion battery modelling featuring a focused ion-beam/scanning electron microscopy based three-phase reconstruction of a $LiCoO_2$ cathode. Electrochim. Acta 115, 131–139.

Klinsmann, M., Rosato, D., Kamlah, M., McMeeking, R.M., 2016. Modeling crack growth during Li insertion in storage particles using a fracture phase field approach. J. Mech. Phys. Solids 92, 313–344.

Koerver, R., Aygün, I., Leichtweiß, T., Dietrich, C., Zhang, W., Binder, J.O., Hartmann, P., Zeier, W.G., Janek, J., 2017. Capacity fade in solid-state batteries: Interphase formation and chemomechanical processes in nickel-rich layered oxide cathodes and lithium thiophosphate solid electrolytes. Chem. Mat. 29, 5574–5582.

Kondrakov, A.O., Schmidt, A., Xu, J., Geßwein, H., Mönig, R., Hartmann, P., Sommer, H., Brezesinski, T., Janek, J., 2017. Anisotropic lattice strain and mechanical degradation of high- and low-nickel NCM cathode materials for Li-ion batteries. J. Phys. Chem. C 121, 3286–3294.

Laresgoiti, I., Käbitz, S., Ecker, M., Sauer, D.U., 2015. Modeling mechanical degradation in lithium ion batteries during cycling: solid electrolyte interphase fracture. J. Power Sources 300, 112–122.

Li, S.E., Wang, B., Peng, H., Hu, X., 2014. An electrochemistry-based impedance model for lithium-ion batteries. J. Power Sources 258, 9–18.

Li, W., Li, M., Hu, Y., Lu, J., Lushington, A., Li, R., Wu, T., Sham, T.-K., Sun, X., 2018. Synchrotron-based X-ray absorption fine structures, X-ray diffraction, and X-ray microscopy techniques applied in the study of lithium secondary batteries. Small Methods 2, 1700341.

Lim, C., Yan, B., Yin, L., Zhu, L., 2012. Simulation of diffusion-induced stress using reconstructed electrodes particle structures generated by micro/nano-CT. Electrochim. Acta 75, 279–287.

Lin, F., Liu, Y., Yu, X., Cheng, L., Singer, A., Shpyrko, O.G., Xin, H.L., Tamura, N., Tian, C., Weng, T.-C., Yang, X.-Q., Meng, Y.S., Nordlund, D., Yang, W., Doeff, M.M., 2017. Synchrotron X-ray analytical techniques for studying materials electrochemistry in rechargeable batteries. Chem. Rev. 117, 13123–13186.

Lin, F., Markus, I.M., Nordlund, D., Weng, T.-C., Asta, M.D., Xin, H.L., Doeff, M.M., 2014. Surface reconstruction and chemical evolution of stoichiometric layered cathode materials for lithium-ion batteries. Nat. Commun. 5, 3529.

Lindqvist, D., 2017. Simulation of Intermittent Current Interruption Measurements on NMC-Based Lithium-Ion Batteries, UPTEC ES, p. 53.

Liu, K., Liu, Y., Lin, D., Pei, A., Cui, Y., 2018. Materials for lithium-ion battery safety. Sci. Adv. 4, eaas9820.

Liu, X.H., Zheng, H., Zhong, L., Huang, S., Karki, K., Zhang, L.Q., Liu, Y., Kushima, A., Liang, W.T., Wang, J.W., 2011. Anisotropic swelling and fracture of silicon nanowires during lithiation. Nano Lett. 11, 3312–3318.

Liu, X.H., Zhong, L., Huang, S., Mao, S.X., Zhu, T., Huang, J.Y., 2012. Size-dependent fracture of silicon nanoparticles during lithiation. ACS Nano 6, 1522–1531.

Lu, Y., Zhang, P., Wang, F., Zhang, K., Zhao, X., 2018. Reaction-diffusion-stress coupling model for Li-ion batteries: The role of surface effects on electrochemical performance. Electrochim. Acta 274, 359–369.

Ma, C., Cheng, Y., Yin, K., Luo, J., Sharafi, A., Sakamoto, J., Li, J., More, K.L., Dudney, N.J., Chi, M., 2016. Interfacial stability of Li metal-solid electrolyte elucidated via in situ electron microscopy. Nano Lett. 16, 7030–7036.

Mai, W., Yang, M., Soghrati, S., 2019. A particle-resolved 3D finite element model to study the effect of cathode microstructure on the behavior of lithium ion batteries. Electrochim. Acta 294, 192–209.

Mao, Y., Wang, X., Xia, S., Zhang, K., Wei, C., Bak, S., Shadike, Z., Liu, X., Yang, Y., Xu, R., Pianetta, P., Ermon, S., Stavitski, E., Zhao, K., Xu, Z., Lin, F., Yang, X.-Q., Hu, E., Liu, J., 2019. High-voltage charging-induced strain, heterogeneity, and micro-cracks in secondary particles of a nickel-rich layered cathode material. Adv. Funct. Mater. 1900247.

McDowell, M.T., Ryu, I., Lee, S.W., Wang, C., Nix, W.D., Cui, Y., 2012. Studying the kinetics of crystalline silicon nanoparticle lithiation with in situ transmission electron microscopy. Adv. Mater. 24, 6034–6041.

McDowell, M.T., Xia, S., Zhu, T., 2016. The mechanics of large-volume-change transformations in high-capacity battery materials. Extreme Mech. Lett. 9, 480–494.

Meijering, E., 2019. https://imagescience.org/meijering/software/featurej/structure/.

Meirer, F., Cabana, J., Liu, Y., Mehta, A., Andrews, J.C., Pianetta, P., 2011. Three-dimensional imaging of chemical phase transformations at the nanoscale with full-field transmission X-ray microscopy. J. Synchrotron Radiat. 18, 773–781.

Mendoza, H., Roberts, S.A., Brunini, V.E., Grillet, A.M., 2016. Mechanical and electrochemical response of a LiCoO$_2$ cathode using reconstructed microstructures. Electrochim. Acta 190, 1–15.

Mirone, A., Brun, E., Gouillart, E., Tafforeau, P., Kieffer, J., 2014. The PyHST2 hybrid distributed code for high speed tomographic reconstruction with iterative reconstruction and a priori knowledge capabilities. Nucl. Instrum. Methods Phys. Res. Sec. B 324, 41–48.

Müller, S., Pietsch, P., Brandt, B.-E., Baade, P., De Andrade, V., De Carlo, F., Wood, V., 2018. Quantification and modeling of mechanical degradation in lithium-ion batteries based on nanoscale imaging. Nat. Commun. 9, 2340.

Natsiavas, P.P., Weinberg, K., Rosato, D., Ortiz, M., 2016. Effect of prestress on the stability of electrode–electrolyte interfaces during charging in lithium batteries. J. Mech. Phys. Solids 95, 92–111.

Newman, J., Thomas-Alyea, K.E., 2012. Electrochemical Systems. John Wiley & Sons.

Ning, G., Haran, B., Popov, B.N., 2003. Capacity fade study of lithium-ion batteries cycled at high discharge rates. J. Power Sources 117, 160–169.

Palacin, M.R., de Guibert, A., 2016. Why do batteries fail? Science 351, 1253292.

Prussin, S., 1961. Generation and distribution of dislocations by solute diffusion. J. Appl. Phys. 32, 1876–1881.

Rao, A.R., Schunck, B.G., 1991. Computing oriented texture fields. CVGIP Graph. Models Image Process. 53, 157–185.

Roberts, S.A., Brunini, V.E., Long, K.N., Grillet, A.M., 2014. A framework for three-dimensional mesoscale modeling of anisotropic swelling and mechanical deformation in lithium-ion electrodes. J. Electrochem. Soc. 161, F3052–F3059.

Rueden, C.T., Schindelin, J., Hiner, M.C., DeZonia, B.E., Walter, A.E., Arena, E.T., Eliceiri, K.W.J.B.B., 2017. ImageJ2: imageJ for the next generation of scientific image data. BMC Bioinform. 18, 529.

Ryu, H.H., Park, K.J., Yoon, C.S., Sun, Y.K., 2018. Capacity fading of Ni-rich Li[Ni$_x$Co$_y$Mn$_{1-x-y}$]O$_2$ (0.6≤x≤0.95) cathodes for high-energy-density lithium-ion batteries: Bulk or surface degradation? Chem. Mat. 30, 1155–1163.

Ryu, I., Choi, J.W., Cui, Y., Nix, W.D., 2011. Size-dependent fracture of si nanowire battery anodes. J. Mech. Phys. Solids 59, 1717–1730.

Sethuraman, V.A., Chon, M.J., Shimshak, M., Van Winkle, N., Guduru, P.R., 2010. In situ measurement of biaxial modulus of Si anode for Li-ion batteries. Electrochem. Commun. 12, 1614–1617.

Shi, F., Song, Z., Ross, P.N., Somorjai, G.A., Ritchie, R.O., Komvopoulos, K., 2016. Failure mechanisms of single-crystal silicon electrodes in lithium-ion batteries. Nat. Commun. 7, 11886.

Smith, K., Wang, C.-Y., 2006. Solid-state diffusion limitations on pulse operation of a lithium ion cell for hybrid electric vehicles. J. Power Sources 161, 628–639.

Song, B., Sui, T., Ying, S., Li, L., Lu, L., Korsunsky, A.M., 2015. Nano-structural changes in Li-ion battery cathodes during cycling revealed by FIB-SEM serial sectioning tomography. J. Mater. Chem. A 3, 18171–18179.

Stein, P., Zhao, Y., Xu, B.-X., 2016. Effects of surface tension and electrochemical reactions in Li-ion battery electrode nanoparticles. J. Power Sources 332, 154–169.

Tjaden, B., Cooper, S.J., Brett, D.J.L., Kramer, D., Shearing, P.R., 2016. On the origin and application of the Bruggeman correlation for analysing transport phenomena in electrochemical systems. Curr Opin. Chem. Eng. 12, 44–51.

Valøen, L.O., Reimers, J.N., 2005. Transport properties of LiPF6-based Li-ion battery electrolytes. J. Electrochem. Soc. 152, A882–A891.

Vasconcelos, L.S., Xu, R., Zhao, K., 2017. Operando nanoindentation: A new platform to measure the mechanical properties of electrodes during electrochemical reactions. J. Electrochem. Soc. 164, A3840–A3847.

Wang, A., Kadam, S., Li, H., Shi, S., Qi, Y., 2018. Review on modeling of the anode solid electrolyte interphase (SEI) for lithium-ion batteries. npj Comput. Mater. 4, 15.

Wang, H., Jang, Y.I., Huang, B., Sadoway, D.R., Chiang, Y.M., 1999. TEM study of electrochemical cycling-induced damage and disorder in LiCoO$_2$ cathodes for rechargeable lithium batteries. J. Electrochem. Soc. 146, 473–480.

Watanabe, S., Kinoshita, M., Hosokawa, T., Morigaki, K., Nakura, K., 2014. Capacity fading of LiAl$_y$Ni$_{1-x-y}$Co$_x$O$_2$ cathode for lithium-ion batteries during accelerated calendar and cycle life tests (effect of depth of discharge in charge–discharge cycling on the suppression of the micro-crack generation of LiAl$_y$Ni$_{1-x-y}$Co$_x$O$_2$ particle). J. Power Sources 260, 50–56.

Wei, C., Zhang, Y., Lee, S.-J., Mu, L., Liu, J., Wang, C., Yang, Y., Doeff, M., Pianetta, P., Nordlund, D., Du, X.-W., Tian, Y., Zhao, K., Lee, J.-S., Lin, F., Liu, Y., 2018. Thermally driven mesoscale chemomechanical interplay in Li0.5Ni0.6Mn0.2Co0.2O$_2$ cathode materials. J. Mater. Chem. A 6, 23055–23061.

Weickert, J., 1999. Coherence-Enhancing diffusion filtering. Int. J. Comput. Vis. 31, 111–127.

Whittingham, M.S., 2008. Materials challenges facing electrical energy storage. MRS Bull. 33, 411–419.

Wu, B., Lu, W., 2019. A consistently coupled multiscale mechanical–electrochemical battery model with particle interaction and its validation. J. Mech. Phys. Solids 125, 89–111.

Wu, Y., Liu, N., 2018. Visualizing battery reactions and processes by using in situ and in operando microscopies. Chem 4, 438–465.

Xia, S., Mu, L., Xu, Z., Wang, J., Wei, C., Liu, L., Pianetta, P., Zhao, K., Yu, X., Lin, F., Liu, Y., 2018. Chemomechanical interplay of layered cathode materials undergoing fast charging in lithium batteries. Nano Energy 53, 753–762.

Xu, R., Sun, H., Vasconcelos, L.S., Zhao, K., 2017a. Mechanical and structural degradation of $LiNi_xMn_yCo_zO_2$ cathode in Li-ion batteries: An experimental study. J. Electrochem. Soc. 164, A3333–A3341.

Xu, R., Vasconcelos, L.S., Shi, J., Li, J., Zhao, K., 2017b. Disintegration of meatball electrodes for $LiNi_xMn_yCo_zO_2$ cathode materials. Exp. Mech. 58, 549–559.

Xu, R., Vasconcelos, L.S., Zhao, K., 2016. Computational analysis of chemomechanical behaviors of composite electrodes in Li-ion batteries. J. Mater. Res. 31, 2715–2727.

Xu, R., Zhao, K., 2016a. Electrochemomechanics of electrodes in Li-ion batteries: A review. J. Electrochem. Energy Convers. 13, 030803.

Xu, R., Zhao, K., 2016b. Mechanical interactions regulated kinetics and morphology of composite electrodes in Li-ion batteries. Extreme Mech. Lett. 8, 13–21.

Xu, R., Zhao, K., 2018. Corrosive fracture of electrodes in Li-ion batteries. J. Mech. Phys. Solids 121, 258–280.

Yang, Y., Xu, R., Zhang, K., Lee, S.-J., Mu, L., Liu, P., Waters, C.K., Spence, S., Xu, Z., Wei, C., Kautz, D.J., Yuan, Q., Dong, Y., Yu, Y.-S., Xiao, X., Lee, H.-K., Pianetta, P., Cloetens, P., Lee, J.-S., Zhao, K., Lin, F., Liu, Y., 2019. Quantification of heterogeneous degradation in Li-ion batteries. Adv. Energy Mater. doi:10.1002/aenm.201900674.

Zhang, S., 2017. Chemomechanical modeling of lithiation-induced failure in high-volume-change electrode materials for lithium ion batteries. npj Comput. Mater. 3, 7.

Zhang, S., Zhao, K., Zhu, T., Li, J., 2017. Electrochemomechanical degradation of high-capacity battery electrode materials. Prog. Mater. Sci. 89, 479–521.

Zhang, S.S., Xu, K., Jow, T.R., 2006. EIS study on the formation of solid electrolyte interface in Li-ion battery. Electrochim. Acta 51, 1636–1640.

Zhao, K., Cui, Y., 2016. Understanding the role of mechanics in energy materials: A perspective. Extreme Mech. Lett. 9, 347–352.

Zhao, K., Pharr, M., Wan, Q., Wang, W.L., Kaxiras, E., Vlassak, J.J., Suo, Z., 2012a. Concurrent reaction and plasticity during initial lithiation of crystalline silicon in lithium-ion batteries. J. Electrochem. Soc. 159, A238–A243.

Zhao, K., Tritsaris, G.A., Pharr, M., Wang, W.L., Okeke, O., Suo, Z., Vlassak, J.J., Kaxiras, E., 2012b. Reactive flow in silicon electrodes assisted by the insertion of lithium. Nano Lett. 12, 4397–4403.

Zhao, Y., Stein, P., Bai, Y., Al-Siraj, M., Yang, Y., Xu, B.-X., 2019. A review on modeling of electro-chemo-mechanics in lithium-ion batteries. J. Power Sources 413, 259–283.